DTIC COPY

REPORT DOCUMENTATION PAGE

Form Approved
OMB No. 0704-01-0188

PLEASE DO NOT RETURN YOUR FORM TO THE ABOVE ADDRESS.

1. REPORT DATE *(DD-MM-YYYY)*	2. REPORT TYPE	3. DATES COVERED *(From - To)*
22-07-2008 2007	REPRINT	

4. TITLE AND SUBTITLE

Nanojets, Electrospray, and Ion Field Evaporation: Molecular Dynamics Simulations and Laboratory Experiments

5a. CONTRACT NUMBER

5b. GRANT NUMBER

5c. PROGRAM ELEMENT NUMBER
61102F

6. AUTHORS
W.D. Luedtke*, Uzi Landman*, Y.-H Chiu, D.J. Levandier#, R. A. Dressler, S. Sok##, and M.S. Gordon##

5d. PROJECT NUMBER
2303

5e. TASK NUMBER
RS

5f. WORK UNIT NUMBER
A1

7. PERFORMING ORGANIZATION NAME(S) AND ADDRESS(ES)

Air Force Research Laboratory /RVBXT
29 Randolph Road
Hanscom AFB, MA 01731-3010

8. PERFORMING ORGANIZATION REPORT NUMBER
AFRL-RV-HA-TR-2008-1120

9. SPONSORING/MONITORING AGENCY NAME(S) AND ADDRESS(ES)

10. SPONSOR/MONITOR'S ACRONYM(S)
AFRL/RVBXT

11. SPONSOR/MONITOR'S REPORT NUMBER(S)

12. DISTRIBUTION/AVAILABILITY STATEMENT
Approved for Public Release; distribution unlimited.

13. SUPPLEMENTARY NOTES
Reprinted from: J. Phys Chem. A (2008) 112, 9628-9649 © 2008, American Chemical Society, *Georgia Inst. Of Technology, Atlanta, GA 30332 #Boston College, 140 Commonwealth Ave., Chestnut Hill, MA, 02167 **Iowa State University, Ames, Iowa 50011

14. ABSTRACT

The energetics, interfacial properties, instabilities, and fragmentation patterns of electrosprays made from formamide salt solutions are investigated in a mass spectrometric vacuum electrospray experiment and using molecular dynamics (MD) simulations. The electrospray is operated in a Taylor cone-jet mode, with the nanojet that forms being characterized by high surface-normal electric field strengths in the vicinity of 1 V/nm. Mass-to-charge ratios were determined for both positive and negative currents sprayed from NaI-formamide solutions with solute-solvent mole ratios of 1:8.4 and 1:36.9, and from KI-formamide solutions with solute-solvent mole ratios of 1:41 and 1:83. The molecular dynamics simulations were conducted on isolated 10 nm NaI-formamide droplets at mole ratios of 1:8 and 1:16. The droplet was subjected to a uniform electric field with strengths ranging between 0.4 and 1/5 V/nm. Both the experiments and simulations demonstrate a mixed charge emission regime where field-induced desorption of solvated ions and charged droplets occurs. The macroscopic parameters, such as average mass-to-charge ratio and maximum surface-normal field strengths deduced from the simulations are found to be in good agreement with the experimental work and consistent with electrohydrodynamic theory of cone-jets. The observed mass spectrometric Na+ and I- solvated ion distributions are consistent with a thermal evaporation process and are correctly reproduced by the simulation after incorporation of the different flight times and unimolecular ion dissociation rates in the analysis.

15. SUBJECT TERMS

Guided-ion beam
Charge transfer
Oxygen-ammonia collisions
Reaction cross section
Hyperthermal reactions

16. SECURITY CLASSIFICATION OF:			17. LIMITATION OF ABSTRACT	18. NUMBER OF PAGES	19a. NAME OF RESPONSIBLE PERSON
a. REPORT	b. ABSTRACT	c. THIS PAGE			Yu-Hui Chiu
UNCL	UNCL	UNCL	UNL		19B. TELEPHONE NUMBER *(Include area code)*

FEATURE ARTICLE

Nanojets, Electrospray, and Ion Field Evaporation: Molecular Dynamics Simulations and Laboratory Experiments

W. D. Luedtke,[†] Uzi Landman,*[,†] Y.-H. Chiu,[‡] D. J. Levandier,[‡] R. A. Dressler,[‡] S. Sok,[§] and M. S. Gordon[§]

School of Physics, Georgia Institute of Technology, Atlanta, Georgia 30332-0430, Air Force Research Laboratory, Space Vehicles Directorate, Hanscom AFB, Massachusetts 01731-3010, and Department of Chemistry, 1605 Gilman Hall, Iowa State University, Ames, Iowa 50011-3111

Received: May 23, 2008; Revised Manuscript Received: July 22, 2008

The energetics, interfacial properties, instabilities, and fragmentation patterns of electrosprays made from formamide salt solutions are investigated in a mass spectrometric vacuum electrospray experiment and using molecular dynamics (MD) simulations. The electrospray source is operated in a Taylor cone-jet mode, with the nanojet that forms being characterized by high surface-normal electric field strengths in the vicinity of 1 V/nm. Mass-to-charge ratios were determined for both positive and negative currents sprayed from NaI−formamide solutions with solute−solvent mole ratios of 1:8.4 and 1:36.9, and from KI−formamide solutions with mole ratios of 1:41 and 1:83. The molecular dynamics simulations were conducted on isolated 10 nm NaI−formamide droplets at mole ratios of 1:8 and 1:16. The droplet was subjected to a uniform electric field with strengths ranging between 0.5 and 1.5 V/nm. Both the experiments and simulations demonstrate a mixed charge emission regime where field-induced desorption of solvated ions and charged droplets occurs. The macroscopic parameters, such as average mass-to-charge ratio and maximum surface-normal field strengths deduced from the simulations are found to be in good agreement with the experimental work and consistent with electrohydrodynamic theory of cone-jets. The observed mass spectrometric Na^+ and I^- solvated ion distributions are consistent with a thermal evaporation process, and are correctly reproduced by the simulation after incorporation of the different flight times and unimolecular ion dissociation rates in the analysis. Alignment of formamide dipoles and field-induced reorganization of the positive and negative ionic charges in the interfacial region are both found to contribute to the surface-normal field near the points of charge emission. In the simulations the majority of cluster ions are found to be emitted from the tip of the jet rather than from the neck region next to the Taylor cone. This finding is consistent with the experimental energy distributions of the solvated ions which demonstrate that indeed most ions are emitted closer to the jet region, that is, beyond the cone-neck region where ohmic losses occur. This observation is also consistent with continuum electrohydrodynamic predictions of cluster-ion evaporation at surface regions of high curvature and therefore maximum surface electric field strengths, which may be the cone-neck region, the breakup region of the jet (usually near the tip of the jet), or the emitted charged droplets. In the nanoscale jets observed in this study, the regions of highest spatial curvature are at the ends of the jets where nascent drops either are forming or have just detached.

1. Introduction

Understanding the fundamental properties of conducting liquids under the influence of applied strong electric fields is a topic of continuing and growing interest. The associated phenomenology governs a number of venerable technological areas, most notably electrospray ionization[1] (see also the Nobel lecture by John Fenn titled "Electrospray Wings for Molecular Elephants"[2]), electrospray propulsion,[3] electrospray painting, inkjet printing,[4] and electrospinning[5] of materials. In all of these applications, the electric field causes deformation and charging of the liquid surface, with consequent phenomena including generation of jets, charged-droplet formation, Coulomb fission, and ion-field evaporation (also referred to as field-induced ion desorption). Most of the above technological applications involve breakup of the original fluid structure (often fluid jet) into droplets, with, possibly, the occurrence of subsequent disintegration processes. Indeed, we note here that the use of electric fields for controlling fluids dates back to (at least) the eighteenth century, with demonstrations of the influence of strong electric fields on the deformation and disintegration patterns of water jets appearing already in 1749,[6] and the employment of electric fields for the deflection of liquid jets described in 1859.[7] The breakup of a charged liquid drop, also called Coulomb fission, was analyzed in 1882 by Rayleigh, who showed that such instability will occur when the forces due to

* Corresponding author. E-mail: uzi.landman@physics.gatech.edu. Tel: (404) 894-3368.
[†] Georgia Institute of Technology.
[‡] Hanscom AFB.
[§] Iowa State University.

10.1021/jp804585y CCC: $40.75
Published on Web 10/02/2008

electrostatic (Coulombic) repulsion of surface charges (expressed as the electrostatic pressure for a charged sphere, $P_E = \sigma^2/2\varepsilon_0$, where σ is the surface charge density and ε_0 is the permittivity of vacuum) exceed the forces associated with the surface tension of the liquid (expressed as the pressure associated with the curvature and surface tension γ of a liquid spherical droplet of radius R, $P_R = 2\gamma/R$). The condition where the two forces are equal is referred to as the Rayleigh instability limit.[8] Rayleigh showed that the charge of a droplet at this limit, with a diameter d, is given by

$$q_R = (8\pi^2\varepsilon_0\gamma d^3)^{1/2} \quad (1)$$

The electric field strength at the droplet surface in the absence of an external field is given by

$$E = \frac{q}{\pi\varepsilon_0 d^2} \quad (2)$$

and the critical field, E_R, is obtained from

$$E_R = \frac{q_R}{\pi\varepsilon_0 d^2} = \sqrt{\frac{8\gamma}{\varepsilon_0 d}} \quad (3)$$

The first observation of the "Rayleigh instability" was reported by Zeleney about thirty years after the work of Rayleigh.[9,10] In these pioneering experiments, Zeleney passed a stream of conducting volatile liquid through a small bore, thin-walled tube, maintained at a high potential relative to an opposing counter electrode. The resulting intense electric field at the tip of the tube dispersed the emanating liquid into a fine spray of charged droplets. Zeleney was able to observe the breakup of the charged droplets as the solvent evaporated (with the remaining droplet thus reaching the stability limit, as predicted by Rayleigh). Seventy years later, Gomez and Tang published some striking photographic records of electrospayed heptane drops undergoing a Coulomb explosion.[11,12]

We note here that although the above prediction for q_R has been reported to agree approximately with most measurements,[13] more refined observations indicate that the instability often occurs at about 80% of q_R.[14-16] The generation of a fine spray via the application of an electric field, as in Zeleney's experiments, is a consequence of the field-induced 'focusing' of fluids into pointed structures, referred to generically as "Taylor cones"; Sir Geoffrey Ingram Taylor was primarily interested in the behavior of water droplets in strong electric fields, such as in thunderstorms.[17] This cone geometry corresponds to the hydrostatic structure in which a balance between the capillary and electrostatic stresses is exactly satisfied on the surface of an equipotential cone. Development of the Laplace equation in polar coordinates leads to the condition $P_{1/2}(\cos\theta) = 0$ on the Legendre function of order $^1/_2$, with the solution $\theta = 49.3°$ (often referred to as the "Taylor angle") for the cone half angle for which the above stress balance is obtained on the conical equipotential surface. For a comprehensive review of the current literature on the fluid dynamics of Taylor cones, see a recent account by Fernandez de la Mora.[18]

Although Taylor's treatment applied to a nonconducting liquid or neutral molecules with dipole moments (for which there is no electric current and no liquid flow), his name continues to be used also in applications where the liquid conducts (due to the presence of charged species, i.e., cations and anions). In the latter case, a thin jet may emerge from the tip of the cone, and it will break up into a series of droplets because of another instability described first by Rayleigh for uncharged liquids[19,20] called a "varicose instability"; this instability has been observed by Plateau in 1872.[21] Underlying this instability are surface tension and capillary effects that are expressed as waves that grow in amplitude until a droplet is pinched off. The accepted mechanism of jet breakup involves flow from regions of the liquid column (cylindrical jet or bridge) with smaller radii, that is, regions of higher curvature (i.e., necks where the Laplace pressure is larger) to neighboring crest regions with lower curvature (and hence lower pressure). Because the resulting curvature in the necks becomes larger and larger as the liquid flows away from this region, the flow of liquid from the shrinking neck to the bulging crest accelerates, leading to a singularity in finite time (namely, the flow velocity diverges), which is accompanied by pinch-off of a droplet (see ref 69 and references cited therein).

Two scenarios for the subsequent evolution of droplets generated via jet breakup have been proposed. The first is the

W. D. Luedtke is a Senior Research Scientist in the School of Physics at the Georgia Institute of Technology and a member of its Center for Computational Materials Science. He received both his undergraduate degrees in Physics and Applied Mathematics in 1976 and his Ph.D. degree in Physics in 1984, from Georgia Tech. His research interests focus on studies of novel behavior of materials at the nanometer scale.

Uzi Landman received his D.Sc. degree from the Israeli Institute of Technology (Technion) in 1969. In 1977 he joined the School of Physics of the Georgia Institute of Technology, where he is a Regents' & Institute Professor, holder of the F. E. Callaway endowed Chair, and Director of the GaTech Center for Computational Materials Science. He authored close to 400 articles in the areas of condensed matter theory, clusters, nanoscience, nanotribology, nanowires, catalysis, quantum dots, microscopic hydrodynamics, and damage mechanisms in DNA, with a focus on the development and application of classical and first-principles quantum computational methodologies.

Yu-Hui Chiu received her Ph.D. degree from SUNY Stony Brook in 1996, studying with Prof. Scott Anderson. After a postdoctoral study with Dr. Kopin Liu at IAMS in Taiwan, and an NRC postdoctoral fellowship with the Air Force Research Laboratory, Space Vehicles Directorate, Hanscom AFB, Massachusetts, she joined the ISR at Boston College in 1999. In 2003 she joined the Air Force Research Laboratory and is currently the task scientist for the Space Chemistry task. Her research area includes ion beam experimentation, electric propulsion, and mass spectrometry.

Dale Levandier obtained his Ph.D. from the University of Waterloo, Canada, in 1990, studying with Giacinto Scoles, and followed this by postdoctoral studies with Jim Farrar, at the University of Rochester, and with Phil Johnson, at SUNY Stony Brook. He currently holds a position as a scientist at the Boston College Institute for Scientific Research in which he performs research for the Air Force Research Laboratory primarily in the area of experimental studies on the dynamics of ion−molecule reactions.

Rainer Dressler obtained his Ph.D. from the University of Fribourg, Switzerland in 1985. After postdoctoral work with Dr. Stephen R. Leone at the University of Colorado, he was hired by the Air Force Research Laboratory at Hanscom AFB, MA. As group leader of the Space Chemistry task, he investigated a broad range of chemical dynamics associated with space flight. In early 2008, Rainer joined Spectral Sciences, Inc., where he continues to pursue his interests in physical chemistry related to space technology and the space environment.

Sarom Sok earned his B.S. with Honors in Chemistry in 2004 from George Mason University as an Early Identification Program Scholar. He is currently a graduate student in the Chemistry department at Iowa State University working under the supervision of Professor Mark S. Gordon. His research focuses on the use of electronic structure methods to study optical properties of excited-state molecules and bonding properties in silicon compounds.

Mark S. Gordon obtained his Ph.D. degree from Carnegie-Mellon University in 1968, studying with John Pople. After postdoctoral study with Klaus Ruedenberg at Iowa State University, he took a position in the Chemistry Department at North Dakota State University, where he rose through the ranks to Distinguished Professor and Chair of the Department. In 1992 he moved to Iowa State University, where he is the Frances M. Craig Distinguished Professor of Chemistry and Director of the Ames Laboratory Applied Mathematical Sciences Program. His research interests focus on electronic structure theory development and applications.

one proposed by Dole and co-workers.[22] Dole's charged residue model (CRM) has been developed to explain experiments on electrically driven jets of a solution of polystyrene molecules, generated by a method (similar to that used earlier by Zeleney) which Dole described in his biography[23] as "I got this idea from learning about the electrospaying of paint onto automobile bodies while working as a consultant for a paint company in Chicago". In the CRM, large charged droplets of volatile liquids will evaporatively diminish in size (that is, reduce their diameters) while maintaining the charge, ultimately reaching the Rayleigh limit and undergoing Coulomb fission; this process is assumed to repeat itself until a charged solute residue is formed.

An alternative model (called the ion evaporation model, or IEM) for the evolution of a large charged droplet subsequent to its generation via jet breakup, has been advanced by Iribarne and Thomson,[24] two meteorologists who were interested in the possibility that charged droplets of seawater might be a source of some of the ions found in the atmosphere. These researchers explored the conditions at which the electric field strength at the surface of the droplet exceeds a threshold value, E_I, at which ion field evaporation occurs. This condition can be met provided $E_I < E_R(d)$ (otherwise Coulomb fission occurs), and the solute residue diameter is less than the critical diameter at which $E_I = E_R(d)$; i.e., in the case of salt solutions the concentration is low. The threshold value E_I derives from the energy to overcome the barrier associated with the combination of the solvation energy of the evaporated ion, and the electrostatic interaction between the ion and the droplet. Iribarne and Thomson[24] estimated that this barrier is approximately 4−5 Å from the droplet surface.

On the basis of a kinetic model and charge mobility experiments, Thomson and Iribarne[25] concluded that the critical field, E_I, was approximately 1 V/nm, and that field evaporation would be expected for droplets with diameters < 10 nm. Loscertales and Fernández de la Mora[26] and Katta and co-workers[27] used charge mobility experiments and refined models to determine electric fields between 0.7 and 1.9 V/nm for the evaporation of different singly charged ions. Fenn et al.[28] also arrived at similar fields by applying a simple electrostatic model to the interpretation of their experiments on dilute polyethylene glycol solutions, assuming that the charges of small droplets are equally spread on the droplet surface, and that the charge distances on the droplet cannot be less than that found on the multiply charged large field-evaporated ions. These authors determined fields ranging from 1.46 to 2.66 V/nm with increasing field strength required for smaller, less charged oligomer ions.

The investigation of the detailed field-evaporation mechanisms from charged droplets is most challenging because a charge-shedding isolated droplet does not ever attain a steady state. The field-induced evaporation phenomenon, however, is not limited to droplets. Indeed, the conditions for field evaporation can also be met at the surface of a flowing electrified jet. The experimental detection and analysis of nascent ion currents from jets requires spray operation under vacuum conditions where conventional ion optics can be used for the analysis of charged particles prior to collisions with a background gas. Because the use of a volatile solvent such as water or methanol in a vacuum would lead to rapid freezing of the jet, the study of field-evaporation from a jet is limited to liquids with low vapor pressures.

In Figure 1 we display schematically different configurations of electrosprays involving a capillary and an extraction electrode.

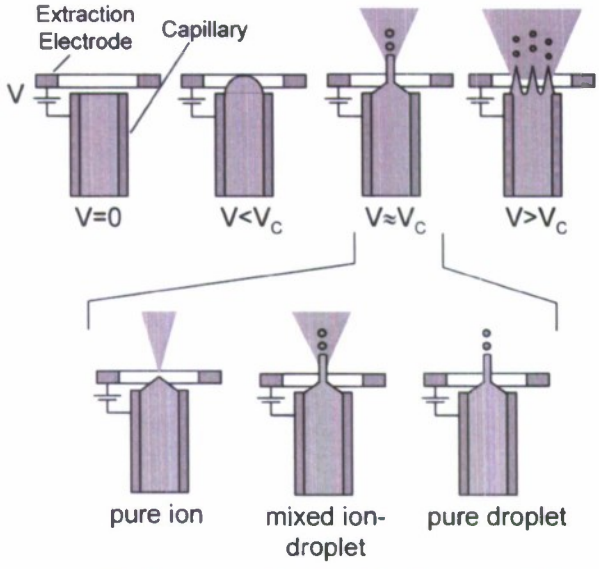

Figure 1. Schematic cross-sectional representation of several configurations and ejection modes of a capillary electrospray. The extraction voltage, V, is applied between an extraction electrode (shaped as a ring) and the capillary containing the conducting liquid (a formamide salt solution in the present study). V_c is the critical extraction voltage at which a Taylor cone is formed. The top row illustrates the liquid response as a function of the extraction voltage; from field-free conditions, to a stressed jet operation, $V > V_c$. The bottom row illustrates the different mixed modes of operation, when the jet is operated in a single cone-jet configuration ($V \approx V_c$). The darkly shaded area outside the orifice of the capillary represents ion emission; this is shown for the case of pure ion emission (leftmost configuration in the bottom row), as well as for a mixed ion-droplet emission mode (middle configuration in the bottom row).

The study of field evaporation on jets is best accomplished at well characterized conditions provided by extraction voltages close to the critical voltage, V_c, at which the Taylor cone that triggers electrospray is formed. Depending on the choice of liquid, operation in this cone-jet configuration can lead to three different modes of charge emission: a pure ion emission mode, a mixed ion-droplet emission mode, and a pure charged droplet emission mode. Liquid metals, having very high surface tensions, and consequently high resistance to Coulomb fission, are known to produce pure, intense metal ion beams in an electrospray configuration with little or no contribution from charged droplets.[29] Jet formation does not occur under typical liquid metal electrospray conditions, and the Taylor cone is stabilized through pure ion emission at the tip of the Taylor cone where the surface normal fields are highest. Solutions involving low-vapor pressure solvents, which are the subject of this work, have significantly more flexible electrospray properties. Such systems generally operate in a mixed ion-droplet emission regime with complex mass spectra of the emitted ions that accompany charged droplets. At normal cone-jet conditions, with the exception of work discussed further below, the ion component represents a very minor fraction of the total emission current. Pure charged droplet emission has only recently been demonstrated[30] by the suppression of ion field evaporation through the choice of solutes with very high solvation energies.

Most of the early work on electrosprays of organic solutions in vacuum was conducted with glycerol. Huberman[31] conducted an energy analysis of positive ions sprayed from a NaI−glycerol solution, and detected a feature that was attributed to metastable solvated ions losing a solvent molecule. Stimpson et al.[32]

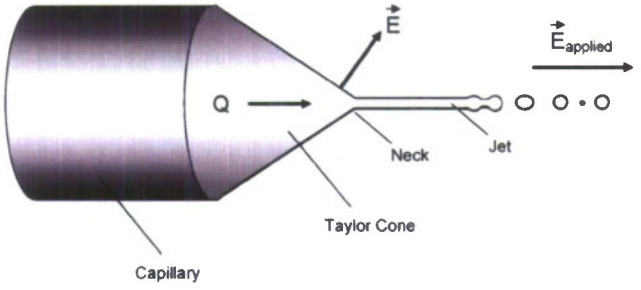

Figure 2. Schematic representation of an electrospray in the cone-jet regime (see Figure 1 for $V \approx V_c$). E represents the surface normal electric field and Q is the volume flow rate. Note the varicose wave on the surface of the jet. The electric field at the neck (E) and the external field ($E_{applied}$) are denoted. In the mixed ion-droplet regime (see the middle configuration in the bottom row of Figure 1) the ejected spray consists of a mixture of droplets and ions (the latter not shown here).

observed similar behavior involving metastable species in a mass spectrometric analysis of both positive and negative ions emitted from glycerol solutions of a number of salts. A large number of solvated ions as well as protonated glycerol ions were detected. In the experiments by Huberman and Stimpson et al., very high extraction voltages, exceeding 8 kV, were used. The high resulting fields are known to generate a stressed jet regime, leading to multiple jets on the rim of the capillary orifice (see top right in Figure 1).[33] In recent years, notable advances have been made in understanding electrosprays operating in the significantly more characterized single cone-jet mode,[34-43] depicted in greater detail in Figure 2. As aforementioned, Taylor[17] showed that the surface tension and electrostatic forces for a nonconducting liquid can balance in a way that leads to formation of a liquid cone. Above a critical field, the cone becomes unstable and a jet is formed; conditions for formation of the cone-jet mode have been discussed[33] early on and most recently Ganan-Calvo[44] described the cone-jet mode as a combination of a slender jet and a static Taylor cone near the capillary (nozzle) orifice. Fernández de la Mora derived a more general theory for single cone-jet sprays of conducting liquids predicting a broader range of cone apex angles which was also confirmed experimentally.[34] The extraction voltages to operate in such a Taylor cone-jet mode are much lower (on the order of 1−2 kV) than those used in the earlier experiments, leading to a significantly gentler break-up of the jet. In ground-breaking work, Fernández de la Mora and Loscertales[35] derived both theoretically and experimentally an expression that gives the proportionality between the parameters of a conducting liquid and the current emitted by the Taylor cone

$$I \sim (\gamma K Q/\varepsilon)^{1/2} \tag{4}$$

where K and ε are the liquid conductivity and dielectric constant, respectively, and Q is the volume flow rate. It is noteworthy that no electrostatic parameters appear in this expression. The role of the external field is the generation of the Taylor cone and the associated surface-charge buildup. Equation 4 can be rearranged and rewritten in terms of the specific charge of the emitted droplets, q/m,

$$\frac{q}{m} \sim \frac{1}{\rho}\sqrt{\frac{\gamma K}{\varepsilon Q}} \tag{5}$$

where ρ is the liquid density. Because droplets formed in jet fission are expected to be charged near the Rayleigh limit, the specific charge is also a measure of the diameter. Thus, eq 5 states that the droplet size emitted by a Taylor cone can be controlled by parameters such as the liquid conductivity and the volume flow rate.

Inspection of the cone-jet structure in Figure 2 allows the identification of three regions: the cone, the jet and the intermediate neck region. The last represents the transition from a flow region in the Taylor cone, in which the electrostatic nonequilibrium associated with the narrowing cone diameter and increasing flow speed leads to ohmic currents within the liquid, to a convective flow region in the jet that is in electrostatic equilibrium, and where the charge density is lowered as the jet speed increases. Thus, the region of highest surface charge and normal electric field is in the intermediate neck region. Gamero-Castaño and Fernández de la Mora[41] derived expressions for the maximum normal electric field and radius of curvature or jet radius in this region:

$$E_{max} = \frac{\gamma^{1/2}}{\varepsilon_0^{2/3}}\left(\frac{K}{Q}\right)^{1/6} \tag{6}$$

$$R_{max} = [\varepsilon_0 Q/K]^{1/3} \tag{7}$$

The above authors were also the first to observe field evaporation from a jet using NaI−formamide solutions.[41] In these experiments, volume flow rates of less than 100 pl/s and conductivities exceeding 1 S/m were required, resulting in electric fields near 1 V/nm, which are consistent with earlier predictions for the electric field values that correspond to the generation of field-induced ion desorption events. Conditions were achieved at which the ion current exceeded the charged droplet current. At these more balanced mixed ion/droplet emission conditions, the curvature of the transition region and the diameter of the jet are predicted to be in the vicinity of 10 nm. This is again in full analogy to the electrospray ionization mechanism postulated for droplets.

Subsequently, ion field evaporation has been commonly observed with a third class of low-vapor pressure liquids, namely, ionic liquids[45-47] (the first two being liquid metals and the organic liquids noted above). Very low flow rates can be obtained by replacing the capillary with a needle etched to optimize wetting properties.[48] Pure ion emission, signifying a vanishing jet, has now been observed for the ionic liquids [Emim][BF_4][47] and [Emim][Im] (Emim, 1-ethyl-3-methylimidazolium; Im, *bis*(trifluoromethylsulfonyl)imide),[49] whereby the former has been successfully sprayed using a microfabricated needle array.[50] In the present paper we focus on formamide salt solutions because of the rich variety of field evaporated ions that are found for these systems, and because they are more computationally tractable, thus allowing systematic comparisons between the experimental measurements and theoretical predictions. Moreover, as demonstrated in several electrospray ionization studies, ion field evaporation at fields near the onset of ion desorption may be viewed as a soft-ionization approach, where the properties of ions produced in this "gentle" desorption process reflect the microscopic properties of the parent solution and its interface, as was assumed in the original analysis by Fenn and co-workers.[28]

Recently, Chiu et al.[47] conducted mass spectrometric analysis of positive ions emitted from a concentrated (28.4 wt %) NaI−formamide solution operated in a Taylor cone-jet, ion field evaporation mode. The measurements identified primarily solvated ions, $Na^+(HCONH_2)_n$, with a preferred solvation number of $n = 4$ (the number of solvating formamide molecules per solvated Na^+), which is the largest solvated ion predicted to be thermally stable with respect to the experimental ion flight times at room temperature. Thus the measurements appear to

confirm the notion of a thermal evaporation process. Interestingly, however, the solvated ion energy distributions were found to be near or below the energies of the charged droplets, contrasting the electrohydrodynamic prediction that ion field evaporation would occur from the neck region of the jet which is expected to have a higher potential than the tip of the jet because of ohmic losses in the cone-jet transition region. Similar observations were made by Gamero-Castaño[43] for the same solution. However, with measurements on the ionic liquid [Emim][Im] in a mixed ion/droplet regime, Chiu et al.[51,52] could demonstrate clearly that field-evaporated ions are emitted at the cone-jet neck, as evidenced by their energy and angular distribution, consistent with theoretical arguments.[41]

Recent experimental and theoretical advances[53−55] have shed new light on the interfacial properties of aqueous salt solutions under conditions free of external electric fields. Counter to the long-held view that atomic ions are repelled by the air/water interface into the bulk, MD simulations of alkali-halide solutions have demonstrated that more polarizable anions reside preferentially at the liquid-to-vacuum interface.[53−59] These results have been confirmed by X-ray photoelectron spectroscopy experiments,[60] as well as sum-frequency[56,57,61,62] and second-harmonic generation experiments[63−67] of aqueous halide solutions at ambient pressure. Though these studies examine the microscopic behavior of static solution interfaces, MD simulations[68] have been conducted on an acidic positively charged water nanodroplet, with the amount of excess charge near the Rayleigh limit. In these simulations, ion field evaporation of hydronium ions was observed; we note here that in these simulations negative ions were not included, and this may influence the properties of the simulated system, particularly at reduced dimensions.

We conclude our brief review of recent work with MD simulations, performed by Moseler and Landman,[69] of liquid flows at nanoscale dimensions, and the formulation of a stochastic hydrodynamic treatment. In these studies, simulations were performed of liquid propane flowing under applied backpressure through a cylindrical tube, and emanating through a nanoscale nozzle into a vacuum; recently, Kang and Landman have extended these simulations to injection of liquid jets into a surrounding fluid.[70] The properties of the resulting jets — in particular the characteristics of the breakup of the liquid jet into droplets — were found to differ from continuum hydrodynamics predictions. It was discovered that a newly derived hydrodynamic formulation that includes intrinsic size-dependent fluctuations, provides a faithfully accurate description, in agreement with the atomistic simulations. This work lays the groundwork for an investigation of electrospray jets, where the cone-jet transition region can be regarded as a virtual nozzle of nanoscale dimensions.

In this paper we present a systematic study of ion field evaporation from salt solutions using a combination of mass spectrometry and MD simulations. To gain insights into the microscopic processes of nanojet formation and charge emission from dielectric liquids under the influence of strong electric fields, we chose to investigate theoretically the behavior and response of liquid drops (made of pure formamide or NaI−formamide solutions) because studies on such systems free us from complicating factors, including considerations of effects due to flow rates, contact angles, and the geometry of the capillary tube or needle, used to generate the slender liquid flowing system; for a discussion of the analogy between cone-jets on an exploding drop and those forming on a meniscus supported by a capillary tube, see the article by Fernandez de la Mora[16] entitled "On the Outcome of the Coulombic Fission of a Charged Isolated Drop". The MD simulations were conducted on a 10 nm diameter, uncharged (equal numbers of positive Na^+ and negative I^- charges) NaI−formamide droplet subjected to external electric fields with strengths on the order of 1 V/nm. The size of the drop was selected such that the corresponding curvature of the droplet ($1/R$) would be comparable to the estimated minimum curvature expected to be encountered on a liquid jet (see eq 7), and thus the physics of jet formation, ion field evaporation, and charge emission from such drops can be taken as a faithful representation of the processes occurring in electric field-driven cone-jet flow systems. Indeed, experimental results of field-induced dual-jet formation on droplets, either flowing through a region of high electric field or levitated, have been reported;[71−74] these studies relied on visual/optical examination and were conducted on droplets with diameters exceeding 50 μm exhibiting formation of jets. Under these conditions, ion field evaporation from the main drop is not expected to occur. We remark here that Grimm and Beauchamp conducted mass spectrometric measurements of field evaporated ions from droplets of a methanol solution that are ejected from larger (170 μm diameter) drops.[74] However, the high external fields that would be required to induce direct field desorption from 10 nm diameter droplets (which, as noted above, is the size range of interest, here) were outside the range of these earlier experiments.

The mass spectrometric measurements presented in this paper were conducted on ions that are field evaporated from a cone-jet of solutions (NaI and KI dissolved in formamide) with similar concentrations to those examined in the simulations. Quantum chemical calculations were carried out to determine the energy-optimal structures and thermochemistry of solvated ion clusters with sizes equal to those observed experimentally. The thermochemistry and associated normal-mode frequencies are used to assess the thermal stabilities and lifetimes of the ions. The solvated ion cluster lifetimes are of particular importance for our analysis because they are used in extrapolating and comparing the simulated results concerning mass distributions of emitted solvated ions (that are simulated for relatively short flight times) to the experimental, mass spectrometric data, obtained for much longer flight times than the simulated ones. Both positive and negative solvated ion distributions, obtained experimentally from respective positive and negative extraction fields, and from calculated evaporation statistics at opposite ends of the simulated droplet, are presented and analyzed.

2. Experimental Section

The mass spectrometric experiment has been described in detail previously,[47] and only the features relevant for this article will be discussed. A schematic of the apparatus is shown in Figure 3. The electrospray source consists of a tapered 5 μm inner diameter fused silica capillary tip (New Objective, Inc.) that is fed by a 50 μm inner diameter transport capillary via a capillary union (Upchurch Scientific). The solution flow rate is controlled by pressurizing the liquid reservoir supplying the transport capillary with dry nitrogen. The flow rate is determined from the velocity of bubbles introduced into the liquid near the transport capillary entrance. The capillary tip is positioned within 1 mm of an extractor electrode with an orifice of 6 mm diameter. The tip and extraction optics are all in a vacuum (10^{-7} Torr). Typical extractor voltages used for the 28.4 wt % NaI−formamide solution were 2 kV. The capillary bias voltage was applied to the capillary through a metal layer that coated both the inner and outer surface of the capillary at the entrance end. Typical

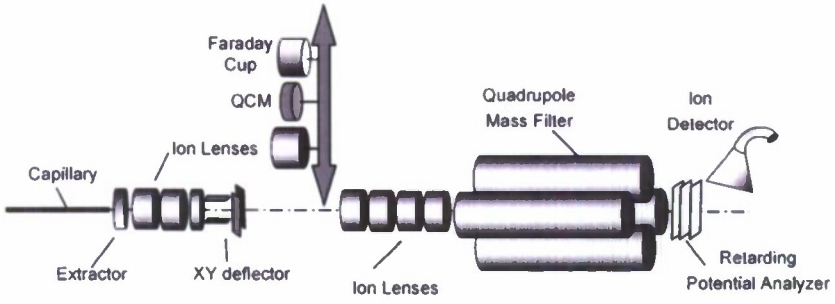

Figure 3. Schematic diagram of the mass spectrometric experiment.

bias potentials were 550 V, whereas the extractor was biased at −1450 V for positive polarity, and the reverse for negative polarity, i.e., −550 and +1450 V. The capillary bias potential was chosen to minimize the ion energy in the mass filter, which is biased at ground potential, while maintaining reasonable ion transmission through the apparatus.

The charged particle beam extracted from the capillary tip can be focused either on a near-field target consisting of an interchangeable Faraday cup, or a quartz crystal microbalance (QCM; XTM/2, Inficon), or toward the entrance of a quadrupole mass filter. The near-field target is used for macroscopic characterization of the charged-particle beam through total current and mass flow measurements. The ratio between mass flow and current provides the average m/q value, which, in conjunction with ion mass distribution measurements, provides a measure of the fraction of charged droplets in the beam. The near-field target is translated away from the beam axis for mass spectral measurements. Given the possibility of broad ion energy distributions, the quadrupole filter is the mass spectrometer of choice because the quadrupole mass setting is independent of energy. However, there is a significant penalty in mass resolution that declines with ion energy. Following transmission through the quadrupole, the ions pass through a retarding potential analyzer prior to being detected using a channel electron multiplier. The retarding potential analyzer is used to measure the energy distribution of mass selected ions.

Mass calibration, the mass transmission function and detector response are obtained from mass spectra of a standard calibrant compound, FC-43, with a known fragmentation pattern at an electron energy of 70 eV. The spectra were obtained after replacing the electrospray source with an electron-impact ionization source. The intensities of fragmented ions of FC-43 were measured for all investigated quadrupole transmission energies, from which the mass-dependent discrimination correction factors were determined.

The concentrated 28.4 wt % and 1/4 volumetrically diluted NaI−formamide solutions used in this study have salt-to-formamide mole ratios of 1:8.4 and 1:36.9, respectively. Similarly, the salt/formamide mole ratios determined for KI−formamide solutions in this study are 1:40.9 and 1:83.0, respectively. The measured conductivities for the concentrated and dilute NaI−formamide solutions are 1.64 and 1.26 S/m, respectively; conductivities of 1.32 and 0.77 S/m are found for the concentrated and dilute KI−formamide solution.

3. Computational Methods

3.1. Molecular Dynamics Simulations. To enable large-scale atomistic simulations of the thermodynamic and electrohydrodynamic properties of complex fluids (with large partial and ionic charges) under the influence of strong electric fields, a computer code with parallel architecture was developed. To model these systems faithfully, it is important to treat the long-range Coulombic interactions accurately and efficiently. In our initial studies of pure formamide droplets, long-range Coulombic interatomic potentials were treated with finite interaction cutoffs ranging from 1 to 4 nm. We found that the employment of finite range cutoffs inhibited the expected droplet elongation as predicted by continuum theory[75] of dielectric drops. Consequently, we concluded that Coulombic interactions must be treated accurately (namely with no cutoff) to bring the simulation results into (at least) qualitative agreement with existing continuum theory. Obviously, the addition of ionic species further increases the necessity of proper implementation of long-range Coulomb interactions. Indeed, the more accurate treatment of dipole−dipole and dipole-field cooperative interactions allows droplets to respond correctly to external fields, including field-induced polarization, elongation, and instabilities that result in emission of charged cluster ions and electrified jets.

In our current simulations the long-range forces are modeled through the use of the fast multipole method (FMM)[76] specifically formulated and programmed for a parallel architecture and adapted to our present system, consisting of an isolated droplet. The FMM algorithm enables the modeling of large systems with long-range interactions by using a "tree-structure" subdivision of cells that allows a charge to interact with a small set of multipoles representing entire, increasingly larger, volumes of remote space, rather than with all of the individual charges contained within the cells. Important features of the program developed for this study are

(1) The ability to replicate basic root-cells and "stack" them along a particular axis to create a long narrow tree-structure. This is particularly useful for efficient simulations of systems such as highly elongated droplets and long liquid jets.

(2) A large degree of flexibility in the choice of boundary conditions (bcs). The computer program allows the implementation of periodic boundary conditions (pbcs) in one, two or three spatial directions, or the execution of "cluster simulations" where pbcs are not imposed altogether. In simulations using pbcs in less than three directions, the nonperiodic directions can be reflecting (closed systems) or absorbing (open system). Absorbing bcs (any atoms that cross the system boundary are removed from the simulation) are necessary in simulations of fragmenting droplets or liquid jets where there are large fluxes of atoms crossing the finite boundaries (keeping these atoms in the root-cell would cause artificial effects).

(3) A modified FMM algorithm so that, when using pbcs, the tree-structure of the root-cell, along with all its computed multipoles, can be replicated a specified number of times as neighboring image cells. When this is done, atoms in the central computational cell see the correct multipole structure as they interact with neighboring periodic image cells out to any desired distance.

(4) The ability to perform constant pressure simulations. The spatial dimensions of the root-cell can be allowed to vary according to a modified constant-pressure algorithm due to Berendsen,[77] while using three-dimensional pbcs and the FMM algorithm. Consequently, bulk samples of both crystals and dielectric fluids with solvated ionic salts at any pressure or temperature of interest, can be prepared and simulated.

In the droplet simulations, the basic root-cell of the FMM code has eight tree levels with the smallest leaf cell chosen to be 1.2 nm on each side. This gives a root-cell of dimension $2^{(8-1)} \times 1.2$ nm = 153.6 nm dimensions on each side. In studies pertaining to the response of the droplet to a constant external electric field, this root-cell was replicated three times along the z-axis (the electric field direction) to give a total tree-structure of 153.6 nm × 153.6 nm × 460.8 nm, with the 10 nm diameter droplet placed in the center. The very large system size allows enough space for the parent droplet to move and elongate freely with sufficient time for charged cluster emission to occur. Once the simulation begins, no temperature control, or control of the droplet center-of-mass motion, are imposed.

Given the size of the present droplets, it is important to utilize an efficient, simple representation of the interatomic forces. Formamide is treated as a solid body with quaternion dynamics,[77] implemented by using a midstep implicit leapfrog algorithm[78] that has been shown to be an extremely stable integration scheme with minimal energy drifts for long simulation periods. The geometry of the formamide molecule is taken from high-resolution X-ray studies of formamide crystals.[79] The AMBER force field parameters[80] were used to describe the intermolecular van der Waals interactions between formamide molecules, the interactions between the formamide molecules and the atomic ions, as well as the ion−ion interactions. CHELP-BOW partial atomic charges[81] were used for the overall description of the electrostatic potential of the formamide molecules. Although long-range Couloumbic interactions between formamide molecules were not truncated, the weak van der Waals interactions were truncated on a group (molecular) basis through the use of a smooth switching function described by Perera et al.[82]

3.2. Quantum Chemical Methods.

3.2.1. Solvated Positive Ions. We have conducted density functional theory (DFT) calculations of the observed positive solvated-ion structures to estimate their thermal stability and the dissociation energies associated with loss of a single formamide solvent molecule. Calculations were performed at the B3LYP/6-31G(d) level using the Gaussian 98/Gaussian 03 quantum chemistry package.[83] Geometries were optimized, and normal-mode frequencies for zero-point energy determinations were calculated for solvated ions of $Na^+(HCONH_2)_n$ and $K^+(HCONH_2)_n$, where $n = 1-6$.

3.2.2. Solvated Negative Ions. Initial geometry optimizations of $[I^-(HCONH_2)_n]$, $n = 1-5$ were performed using an augmented correlation consistent double-ζ basis set for second row atom,[84] 6-31G basis set for hydrogen,[85] Radom ECP basis set for iodine,[86] and the B3LYP[87−89] functional. The treatment of negative cluster ions required a higher level of theory due to the significantly higher degree of correlation, and thus the geometries were refined with Møller−Plesset second-order perturbation (MP2) theory[90−92] and the 6-311+G(d,p)[93] basis set using the Radom 6-311+G(df) basis set for iodine.[94] Gradient convergence tolerance for geometry optimizations was set to 10^{-6} hartree/bohr. Stationary points were characterized by a positive definite Hessian (matrix of energy second derivatives). Harmonic zero-point energy and temperature corrections (to 298.15 K) were obtained using the MP2 Hessians. All calculations were performed using the June 27, 2005 (R3) version of GAMESS (General Atomic and Molecular Electronic Structure System).[95,96]

3.3. Unimolecular Ion Dissociation Rate Calculations. The distributions of the measured ion solvation numbers (that is, the distribution function of the number of solvating formamide molecules in a solvated-ion cluster) deduced from the measurements, are compared with predictions based on the assumption that the ions are evaporated from a liquid at or near room temperature. The internal energy of a solvated ion increases with solvation number, and the dissociation energy (that is, the energy associated with the loss of a single solvent molecule) declines upon increased solvation. Above a certain solvation number, the average internal energy exceeds the dissociation energy of the solvated ion, leading to high dissociation rates in relation to the experimental and simulation time scales. Given the relatively short flight times of ~30 μs of ions in our mass spectrometer, it is possible that metastable ions, i.e., those with internal energies above the dissociation limit, reach the detector prior to dissociating. To assess the fractions of the observed ions that are produced with internal energies above the dissociation limit, and to substantiate the present interpretation that ion field evaporation is comparable to a thermal evaporative process, we have conducted RRKM unimolecular dissociation rate calculations of ions near the thermal stability limit at room temperature.

Using the normal-mode frequencies from the ab initio calculations, we determine the thermal internal energy distributions of the observed solvated ions from the relation

$$F(E_{int})\,dE_{int} = F_{rot}(E_{rot})\,F_{vib}(E_{vib})\,dE_{rot}\,dE_{vib} \quad (8)$$

where $F_{rot}(E_{rot})$ and $F_{vib}(E_{vib})$ are the normalized rotational and vibrational Maxwell−Boltzmann energy distribution functions for a temperature, T, and

$$E_{int} = E_{rot} + E_{vib} \quad (9)$$

For those ions with internal energies exceeding the binding energy, we determine the unimolecular dissociation rate using a RRKM approach, following the methodology developed by Hase and co-workers.[97] Due to the large dipole of formamide (3.7 D) and the resulting strong attractive interaction between the solvated ion and the solvating ligands, there is no centrifugal barrier to dissociation and a very loose transition state is assumed. We assume conditions near the phase space limit, and the transitional vibrational modes are treated as rotors, following Rodgers et al.[98] All systems considered include a single solvation shell and, given the shallow global minima and near symmetry of the normal-mode frequencies, all ligands are treated equivalently. All rotors are treated as active in both the reactant and transition states, vibrational states are treated as harmonic oscillators, and the sum and density of states are determined using the Beyer−Swinehart direct count algorithm.[99] Adiabatic treatment of both reactant and transition-state rotors does not markedly change the results. Furthermore, given the "loose" nature of the transition state, we find that the results are not sensitive to the definition of the transition state (i.e., the distance of the dissociating ligand with respect to the ionic center).

The survival fraction, $P(n,T)$, of ions of a particular solvation number, n, at a temperature, T, is then determined from the expression

$$P(n,T) = P_s(n,T) + \int_{E_0}^{\infty} P_m(n,T,E_{int})e^{-k(E_{int})\tau}\,dE_{int} \quad (10)$$

where $P_s(n,T)$ is the fraction of stable ions with internal energies

TABLE 1: Electrospray Source Parameters of the Experimentally Investigated NaI−Formamide Solutions[a]

NaI mole ratio: conductivity:	1:8.4 1.64 S/m		1:36.9 1.26 S/m	
extraction voltage (V)	2000	2000	2400	2400
polarity	+	−	+	−
I(total) (nA)	250	464	120	200
I(Faraday cup) (nA)	28	58	63	60
$\dot{m}$(QCM)(ng s^{-1})	2.4	3.0	5.4	4.0
m/q(Daltons)	8410	4930	8330	6360
E_{max}(V/nm)	1.70	1.64	1.42	1.49
R_{max}(nm)	2.30	2.48	3.29	2.98

[a] I(total) and I(Faraday cup) correspond to the total emission and Faraday cup currents, respectively. $\dot{m}$(QCM) is the mass flow as measured on the QCM. E_{max} and R_{max} correspond to the maximum electric field strength and the associated radius of curvature at the jet neck given by eqs 6 and 7.

below the dissociation limit, E_0; $P_m(n,T,E_{int})\,dE_{int}$ is the fraction of ions with energies in an interval $E_{int} + dE_{int}$; $k(E_{int})$ is the unimolecular dissociation rate constant, and τ is the average flight time of the respective ions in the mass spectrometric apparatus described in section 2. The experimental flight times are on the order of 25 μs.

4. Results

4.1. Mass Spectrometric Measurements. The concentrated and dilute NaI−formamide solutions were electrosprayed in a Taylor cone-jet mode. The operational parameters of the experiments are summarized in Table 1. For the 1:8.4 mol ratio solution, the extraction voltage was 2000 V for both polarities, whereas a slightly higher voltage was necessary for stable operation of the more dilute 1:36.9 solution. The measured charge emission currents correspond to I(total) in the Table 1. Mass flows registered by the QCM detector are also listed. The average charged particle mass-to-charge ratio, m/q, is then derived from the ratio of mass flow to Faraday cup current. The comparison between the total emission current and the Faraday cup current which collects at a solid angle close to that of the QCM, allows an assessment of the electrospray divergence. The markedly higher divergence observed for the concentrated solution can be attributed to the lower acceleration voltage, the higher current density, as well as the possibility of changing electrospray dynamics. This will be further addressed in the discussion (see section 5).

The relatively low m/q values suggest that both solutions are sprayed in a mixed droplet/ion emission regime, where the main fraction of mass flow is carried by the droplets, and a substantial fraction of the current comes from ions. This indicates that the present Taylor cone-jets operate at dimensions where ion field evaporation occurs. Field evaporation is further verified by the determination of the maximum electric field strength and the corresponding characteristic radius of curvature according to eqs 6 and 7. The flow rates, Q, were obtained from the mass flow assuming a density of 1.13 g cm^{-3}. The surface tension of pure formamide, 0.0575 N m^{-1}, was assumed for the calculation of E_{max}. Note that eqs 6 and 7 are based on the total flow rate so that the derived values based on the QCM registered mass flow must be regarded as upper (E_{max}) and lower (R_{max}) limits. Depending on the charge emission dynamics, it is possible that nonuniformity exists in the angular m/q distributions, thereby causing differences between m/q values determined on axis, as with the present near-field probe, compared to those obtained from the total current and mass flow. The representative maximum electric field strength ranges from 1.42 to 1.7 V/nm, with higher fields derived for the concentrated solution, whereas the jet dimensions are associated with radii in the range between 2.3 and 3.29 nm, with the largest radii determined for the dilute solutions.

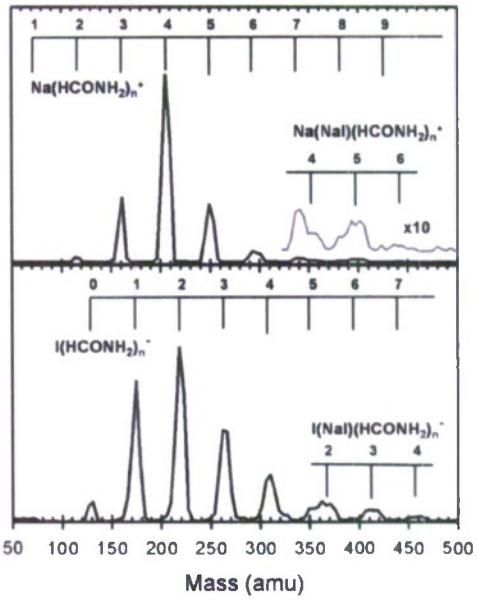

Figure 4. Sample positive and negative ion mass spectra observed from the vacuum electrospray of a concentrated (28.4 wt %) NaI−formamide solution. Solvation number assignments are shown for solvated and complex ion structures.

The negative total emission currents tend to be almost twice as high as those observed for positive charge emission. Two significant differences are observed for the dilute solution in comparison with the concentrated solution: (i) the total emission current is lower, and the fractional current registered on the Faraday cup is higher, signifying a less divergent spray, and (ii) the negative ion average mass-to-charge ratio is higher for the dilute solution, whereas the positive ion mass-to-charge ratio does not change significantly upon dilution.

Figure 4 shows positive and negative ion mass spectra recorded for the 1:8.4 NaI−formamide solution. The spectra have been corrected with respect to the mass spectral transmission function. The low mass resolution can be attributed to the high transmission energies of 550 eV. The most abundant positive ion mass can be attributed primarily to solvated sodium ions, $Na^+(HCONH_2)_n$, with the $n = 4$ solvated ion being the most abundant positive ion species. Trace abundances of ions attributed to solvated ions including an ion pair, $Na^+(NaI)(HCONH_2)_n$, are also observed. Such complex ions are not detected with a positive polarity in the electrospray mass spectrum of the 1:36.9 solution. The mass resolution is insufficient to fully resolve the ions including an ion-pair from the simple solvated ions. The individual abundances are determined by deconvoluting the data using fits of Gaussian peak shapes given by the experimental resolution and centered at the expected mass positions. The derived normalized abundances are shown for the two concentrations in Figure 5a,b. The abundances of the simple solvated ions are essentially identical for the two concentrations except for higher abundances at the highest solvation numbers in case of the more dilute solution.

When operated in a negative mode, the main observed ions are solvated iodine anions, $I^-(HCONH_2)_n$, with a distribution peaking at $n = 2$ in the mass spectrum observed for the concentrated (1:8.4) solution (Figure 4). Solvated ions including

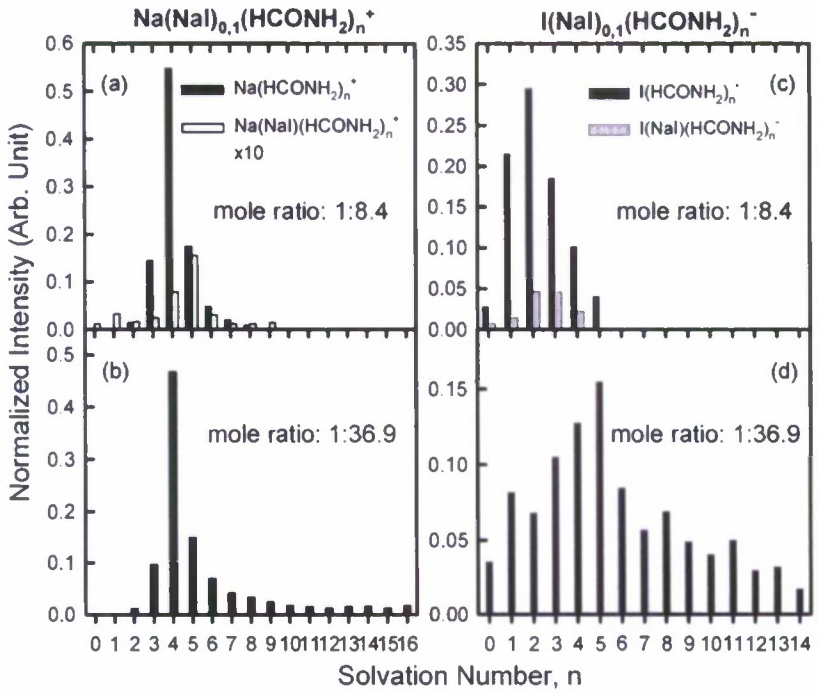

Figure 5. Na^+ solvation number distributions derived from the mass spectra of (a) 1:8.4 (top) and (b) 1:36.9 (bottom) mole-ratio NaI−formamide solutions. I^- solvation number distributions derived from the mass spectra of (c) 1:8.4 (top) and (d) 1:36.9 (bottom) mole-ratio NaI−formamide solutions.

ion-pairs $I^-(NaI)(HCONH_2)_n$, are also observed. The abundances following deconvolution are shown in Figure 5c,d. Contrary to the Na^+ positive ions, dilution has a marked effect on the observed solvated I^- mass spectrum. The distribution of simple solvated ions becomes significantly broader upon dilution, and it peaks at a higher solvation number, $n = 5$. As with the positive ions, the complex ions, $I^-(NaI)(HCONH_2)_n$, are not detected upon dilution.

Although no simulations were carried out for KI solutions, we found it useful for comparative purposes to also investigate mass spectrometrically KI−formamide solutions. The KI−formamide solution could not be electrosprayed at the same concentration (28.4 wt %) used for the NaI−formamide solution due to problems caused by crystallization in the capillary orifice region. Stable Taylor cone-jets were produced with KI-formamide mole-ratios of 1:41 and 1:83 at extraction voltages of 2100 and 2300 V, respectively. Simple and complex solvated ions were observed, as for the NaI−formamide system. The abundances are shown in Figure 6a−d. Similar to the Na^+ solvated ion distributions, dilution results in only a minor change in the K^+ solvation number distributions. A small shift toward lower solvation numbers is found upon dilution. However, the distributions (that peak near $n = 5$) extend to significantly higher solvation numbers compared to the Na^+ distributions discussed above, and they may continue to even larger solvation numbers but are truncated by the range of our quadrupole mass spectrometer. Complex ions, $K^+(KI)(HCONH_2)_n$, are generally more abundant than in the NaI solutions, and they appear to be more abundant for the dilute solution. The solvated anion distributions show the same trend of peaking at higher solvation numbers upon dilution as observed for the NaI solutions. Contrary to the dilute NaI solution, for the KI case complex anions appear to be more abundant upon dilution.

Figure 7 compares the retarding potential measurements of energy distributions per unit charge of mass-selected $Na^+(HCONH_2)_4$ ions with high mass charges (m/q > 400 amu), obtained by operating the quadrupole in a radio-frequency-only high-pass mode. The capillary potential was biased at 550 V while the retarding grid analyzer was at ground. The data show that high mass charged particles correspond most likely to charged droplets and are formed at a potential ~200 V below the capillary or bulk liquid potential, whereas the solvated ions are formed with a broader energy distribution centered slightly below the droplet appearance energy, with a minor contribution at higher energies. Very similar distributions were obtained for ions with other solvation numbers; at the same time, the energy distributions do not change noticeably for negative ions and for varying dilutions.

4.2. Solvated Ion Thermochemistry and Ion Survival Fractions. Calculated global minimum structures of several solvated ions are shown in Figures 8 and 9; the geometrical parameters for the optimized structures of $Na(HCONH_2)_n^+$, $n = 1-4$, and $I(HCONH_2)_n^-$, $n = 1-5$, are given in the Appendix, Tables A1 and A2, respectively. The binding energies of the calculated solvated ions, $Na(HCONH_2)_n^+$, $n = 1-6$, $K(HCONH_2)_n^+$, $n = 1-6$, and $I(HCONH_2)_n^-$, $n = 1-5$, determined from the quantum chemical calculations, are shown in Table 2. Also listed are the zero-point energies, E_{zpe}, and the internal energies, E_{int}, above the zero-point energies at 298.15 K (difference between thermal energy and zero-point energy). It is seen that the internal energy at 298.15 K exceeds the binding energy for ions with a solvation number above $n = 4$ for the cationic solvated ions (Na^+ and K^+), and above $n = 3$ for the I^- solvated ions, respectively. Thus solvated ions with n above the solvation numbers limits are thermally unstable and given sufficient time they will dissociate, desorbing a formamide molecule.

Lifetimes of ions with solvation numbers near the thermal stability limit were calculated for Na^+ and I^- solvated ions. Table 3 lists the thermal ion survival fractions calculated for selected $Na^+(HCONH_2)_n$ ions evaporated with characteristic temperatures of 300, 350 and 400 K. The survival fractions are

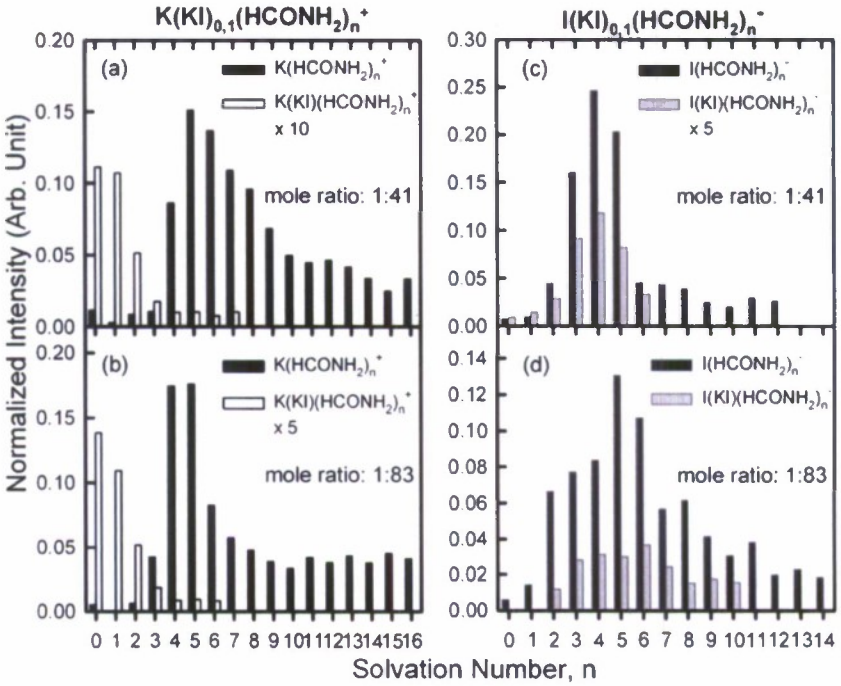

Figure 6. K^+ solvation number distributions derived from the mass spectra of (a) 1:41 (top) and (h) 1:83 (hottom) mole-ratio KI−formamide solutions. I^- solvation number distributions derived from the mass spectra of (c) 1:41 (top) and (d) 1:83 (bottom) mole-ratio KI−formamide solutions.

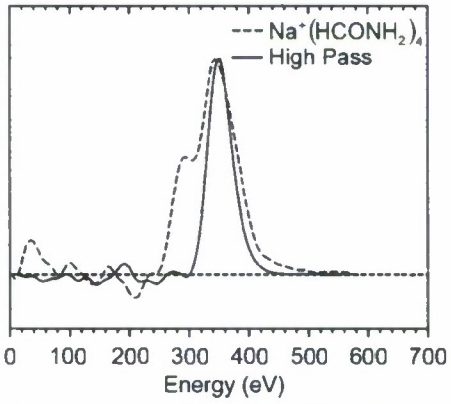

Figure 7. Retarding potential measurements of solvated ion and droplet (corresponding to high pass, m/q > 400) energy distributions. The capillary potential was biased at 550 V, and the analyzer was at ground.

calculated for infinitc observation times and mass spectrometer flight times and are based on the unimolecular dissociation rate calculations described in section 3.3. Table 4 lists corresponding survival fractions for selected $I^-(HCONH_2)_n$ ions.

4.3. Molecular Dynamics Simulations. Neutral dielectric and charged droplets and their response to uniform electric fields have been of great interest for a rather long time for both fundamental scientific reasons and technological ones.[8,17,71−74] The salient features of the physics associated with electrosprays operating in the cone-jet mode may be seen already in the simpler problem of a conducting liquid droplet elongated in a uniform external electric field, including the formation of electrified jets, as well as the emission and acceleration of charged species at the ends of the elongated parent drops. Indeed, Taylor[17] studied the instabilities and jet formation of fluids emerging from an electrospray device as a way to investigate in a more controlled manner the physics related to the elongation and jet formation of droplets in a uniform electric field.

In light of the above we initiated atomistic molecular dynamics simulation studies, aiming at exploration of field-induced fluid instabilities relevant to the operation of electrospray devices hy studying first the closely related phenomena present in the behavior of dielectric droplets, with and without dissolved salts. As discussed below, the results of the MD simulations, which are found to agree well with the experimental electrospray results measurements, provide deep insights into the physical origins of the ohserved behavior. As a prelude to our discussion of the NaI−formamide solution droplets that are our primary focus, we present in section 4.3.1 results for pure formamide droplets which are taken to have the same size as the NaI−formamide solution droplets which we analyze in section 4.3.2.

4.3.1. Simulations of Pure Formamide. Because the interatomic and intermolecular interaction potential parameters employed in our simulations were not specifically developed to reproducc certain physical properties of the simulated formamide (such as the melting point and dielectric constant), we performed first exploratory simulations that allow us to assess the physical properties of the simulated liquid and the faithfulness of the simulation model. Constant pressure simulations and liquid−solid coexistence studies[100] indicate that our description of formamide yields a liquid density that is to within a few percent of the experimental value, and a melting point that is approximately 10 K above the experimental value of 275 K. For an improved comparison with experiment, and to avoid freezing of the field-evaporating salt solution droplets, the simulations are, therefore, performed at 310 K (that is, 10 K above the experimental conditions).

The droplets used in our simulations were created hy "carving out" a spherical region from an equilibrated bulk liquid simulation that was performed at constant temperature and zero pressure, with a subsequent equilihration prior to the application of an external field. The diameter of the spherical droplet chosen for the MD simulations is 10 nm and it contains 7150 formamide

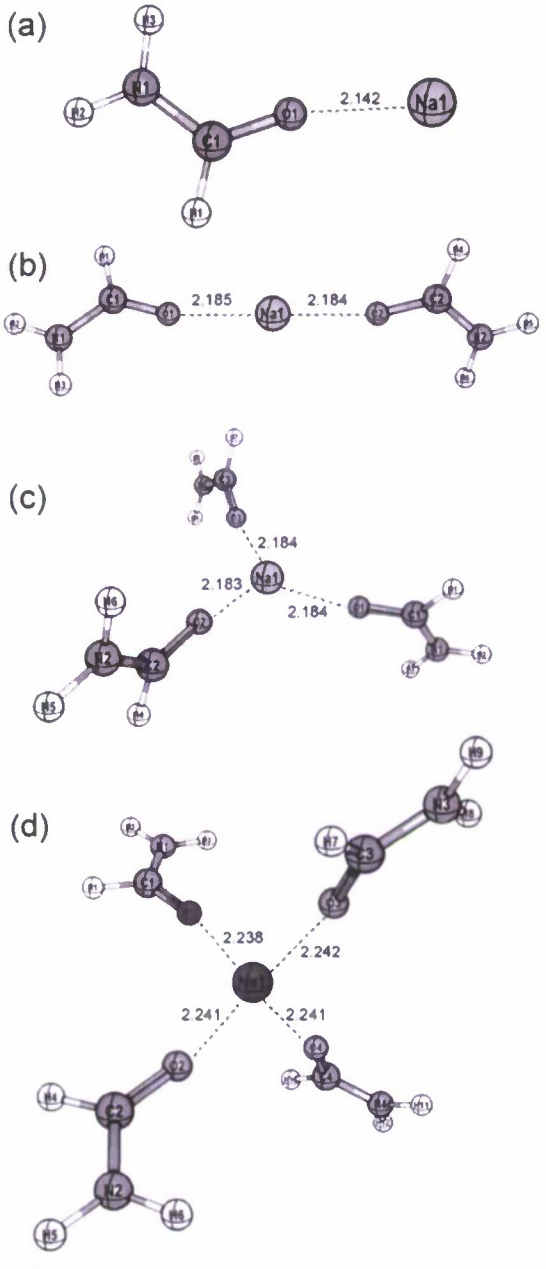

Figure 8. (a)−(d) $Na^+(HCONH_2)_n$, $n = 1-4$, optimized solvated ion structures calculated at the B3LYP/6-31G(d) level.

molecules (each molecule composed of six atomic partial charges). This droplet is large enough to allow meaningful comparison with continuum electrohydrodynamic theories, and in addition its curvature is similar to the estimated local curvature of the experimentally probed liquid jet at the location where the electric field strength is maximal (see eqs 6 and 7). From a practical point of view, the chosen droplet size is sufficiently small to allow a wide range of computer experiments to be performed in a reasonable amount of time.

The droplet was equilibrated in a range of increasing electric field strengths (from 0 to 3 V/nm). The effect of the externally imposed electric field is depicted in Figure 10, where we display snapshots of the droplet for three values of the applied field, illustrating instability at a critical electric field strength. At field strengths below ~0.5 V/nm, the droplet undergoes mild elongation with increasing field strength. At a field strength of 0.625 V/nm the droplet becomes unstable and undergoes a pronounced elongation, resulting in a change in aspect ratio η

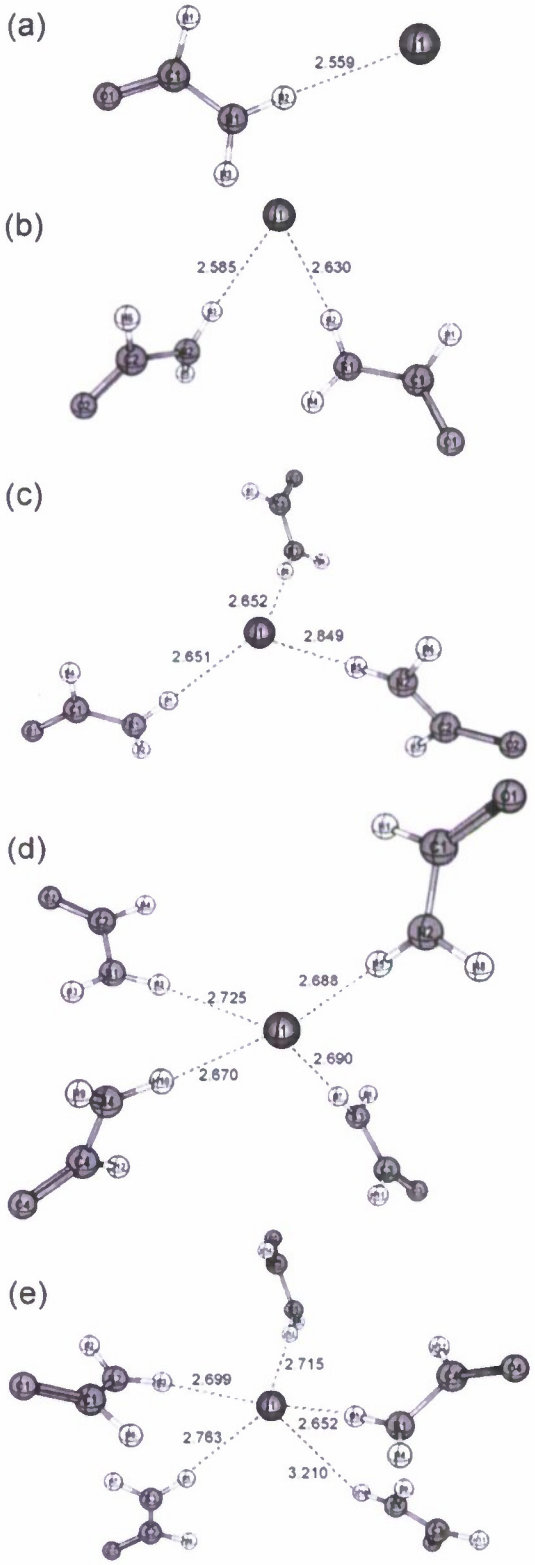

Figure 9. (a)−(e) $I^-(HCONH_2)_n$, $n = 1-5$, optimized solvated ion structures calculated at the MP2/6-311+G(d,p) level.

$= c/a$ (where c and a are the semimajor and semiminor axes of a prolate ellipsoidal fit to the droplet shape) from $\eta \sim 2$ to $\eta \sim 12$. The elongation is also reflected in changes in the average molecular dipole moment projected onto the z axis. There have been a number of studies addressing the critical external field at which a dielectric droplet displays this instability. In early work, Taylor[17] theoretically predicted that a droplet of initial

TABLE 2: Thermochemistry of $Na^+(HCONH_2)_n$, $n = 1-6$, $K^+(HCONH_2)_n$, $n = 1-6$, and $I^-(HCONH_2)_n$, $n = 1-5$, Solvated Ions Determined with the Indicated ab Initio Methods[a]

	B3LYP/6-31G(d)		
n	E_{zpe}	E_{int}	$D(MF_{n-1}-F)$
	$Na^+(HCONH_2)_n$		
1	30.1	3.33	39.7
2	59.9	6.71	33.3
3	89.4	10.3	24.1
4	118.4	14.0	17.2
5	149.5	16.3	15.7
6	178.2	20.2	7.2
	B3LYP/6-31G(d)		
n	E_{zpe}	E_{int}	$D(MF_{n-1}-F)$
	$K^+(HCONH_2)_n$		
1	29.8	3.46	28.7
2	59.3	7.02	24.0
3	88.7	10.6	19.5
4	117.7	14.4	15.6
5	148.8	16.8	14.4
6	178.3	20.3	10.8
	MP2/6-311+G(d,p)		
n	E_{zpe}	E_{int}	$D(MF_{n-1}-F)$
	$I^-(HCONH_2)_n$		
1	27.8	3.6	17.4
2	56.0	7.0	14.9
3	83.7	10.8	12.1
4	111.8	14.3	10.9
5	140.0	17.1	8.4

[a] The internal energy, E_{int}, signifies the 298.15 K thermal energy above the zero-point energy, E_{zpe}. The binding energy, $D(MF_{n-1}-F)$, refers to the loss of a single solvent molecule, F=$HCONH_2$. All values are given in kcal/mol.

TABLE 3: Survival Fractions for Selected $Na^+(HCONH_2)_n$ Ions Evaporated with Characteristic Temperatures of 300, 350 and 400 K[a]

t	$n = 4$	$n = 5$	$n = 6$
	$T = 300$ K		
∞	0.927	0.503	8.0×10^{-5}
MS (26, 28, 31 μs)	0.994	0.662	1.0×10^{-4}
	$T = 350$ K		
∞	0.702	0.148	0.000
MS (26, 28, 31 μs)	0.920	0.279	0.000
	$T = 400$ K		
∞	0.332	0.035	0.000
MS (26, 28, 31 μs)	0.718	0.070	0.000

[a] The survival fractions are listed for infinite observation times, t, and flight times through mass spectrometric experiment (MS).

radius R (in zero external field) becomes unstable at an external field strength, $E_{critical}$, satisfying (MKS units):

$$E_{critical} = 1.625(\gamma/2\pi\varepsilon_0 d)^{1/2} \quad (11)$$

Using $\gamma = 0.046$ N/m for the surface tension of the simulated droplet (computed in separate simulations)[100] and $d = 9.68$ nm for the computed equimolar diameter results in a predicted critical applied electric field $E = 0.48$ V/nm, which is only slightly lower than the interval of 0.5−0.625 V/nm in which the instability is observed to occur in the MD simulation; we note that if the experimental surface tension[101] $\gamma = 0.0575$ N/m is used, the predicted critical field strength is 0.53 V/nm. We conclude that a continuum formalism provides an adequate description of our results obtained for nanometer scale droplets. Additionally, it was discovered[100] that at higher electric fields (about 1.4 V/nm) field-induced crystallization of the pure formamide droplet occurs.

TABLE 4: Survival Fractions for Selected $I^-(HCONH_2)_n$ Ions Evaporated with Characteristic Temperatures of 300, 350 and 400 K[a]

t	$n = 3$	$n = 4$	$n = 5$
	$T = 300$ K		
∞	0.859	0.295	0.036
MS (29, 32, 34 μs)	0.957	0.548	0.091
	$T = 350$ K		
∞	0.620	0.088	0.006
MS (29, 32, 34 μs)	0.811	0.224	0.016
	$T = 400$ K		
∞	0.341	0.023	0.000
MS (29, 32, 34 μs)	0.570	0.067	0.001

[a] The survival fractions are listed for infinite observation times, t, and flight times through mass spectrometric experiment (MS).

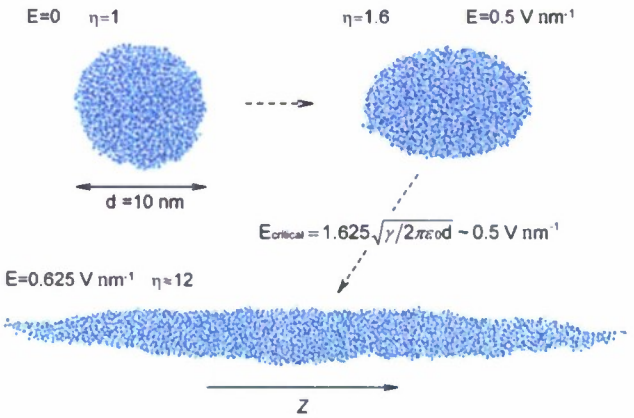

Figure 10. Atomic configurations taken from a molecular dynamics simulation of a 10 nm formamide droplet prior to and after the application of an electric field. The formamide molecules are depicted in blue. When a critical field is exceeded, the droplet deforms to an ellipsoidal stable configuration. The critical field is calculated for a 10 nm diameter droplet and assumes a surface tension of 0.046 N/m. For larger fields, highly elongated shapes with sharply pointed ends develop along the field direction. The aspect ratios, η, for the various configurations are specified. The Z-axis points in the electric field direction.

4.3.2. Simulations of 10 nm NaI−formamide droplets. Having illustrated that the thermodynamics and phase behavior of a dielectric droplet can be modified and manipulated through the use of external electric fields, we turn next to investigations of formamide droplets with a dissolved NaI salt at concentrations that are comparable to those used in the experiments described in section 4.1. Simulations were performed on 10 nm NaI−formamide solutions with NaI−formamide ratios of 1:8 and 1:16, respectively in fields of 0.5, 0.625, 0.75, 1.0 and 1.5 V/nm. The concentrated droplets contain 7150 formamide molecules and 900 dissolved NaI units, corresponding to a 29 wt % solution that is nearly identical to the concentrated solution used in the experiments. The salt solution droplets were prepared similarly to the pure formamide droplets described above.

Snapshots of the 1:16 salt solution droplet subjected to an electric field of 0.625 V/nm are shown in Figure 11. A stage of initial elongation along the field direction is shown in Figure 11b, 400 ps after the field has been turned on. Figure 11c, taken

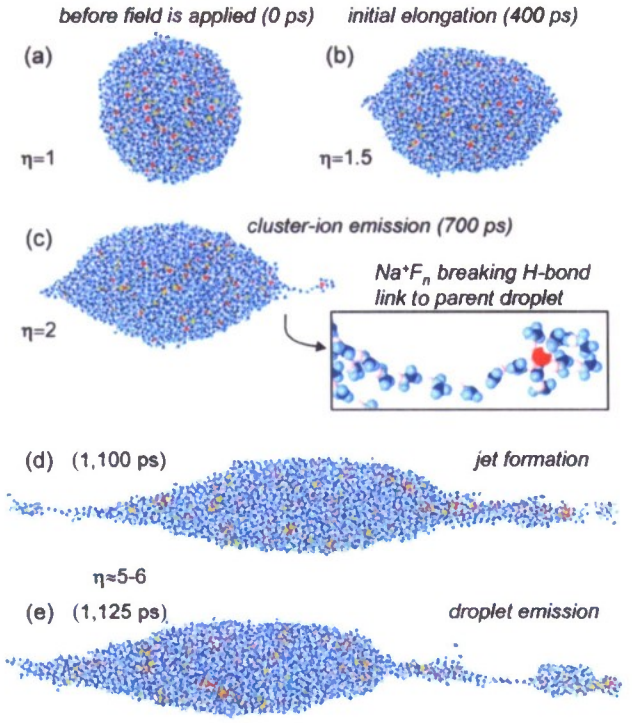

Figure 11. Atomic configurations taken from a molecular dynamics simulation of a 10 nm diameter droplet of a 1:16 NaI−formamide solution, selected during different stages of elongation following the application of a uniform external electric field of 0.625 V/nm. Na^+ and I^- ions are shown as red and yellow spheres respectively, and formamide (F) molecules are in blue. In the inset for $\eta = 2$, showing a hydrogen-bond connected "molecular wire", the oxygen atom of the formamide molecule is shown in pink, the hydrogens in light blue, the carbon in light green, the nitrogen in dark blue. (d) and (e) show formation of a nanojet and subsequent emission from its tip of nanoscale clusters of ions solvated by formamide molecules. Time is measured (in ps) with respect to the instant when the field is turned on ($t = 0$): (a) 0; (b) 400 ps; (c) 700 ps; (d) 1100 ps; (e) 1125 ps. The aspect ratios, η, for the various configurations are also indicated.

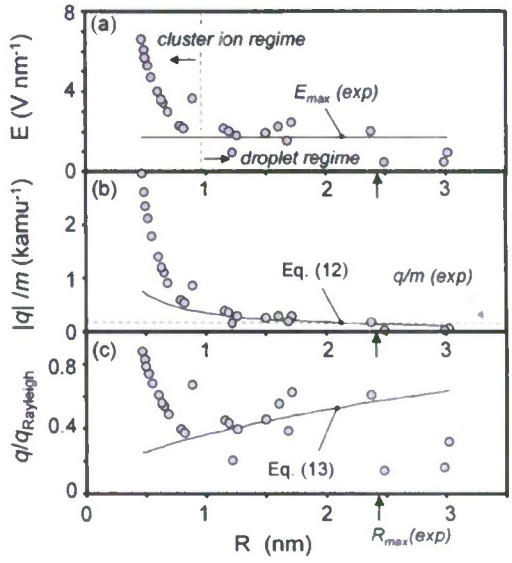

Figure 12. Properties of the charged clusters emitted from the droplet described in Figure 11 as a function of cluster radius: (a) the estimated electric field at the droplet surface, (b) the charge-to-mass ratios and (c) the observed (MD) charge divided by the predicted charge for Rayleigh instability and fission. The dashed and solid lines compare MD results to estimates based on the experimental electrospray results (from Table 1; see text for details).

300 ps later, exhibits further elongation of the droplet, and the onset of charge emission in the form of a Na^+ solvated ion. In the snapshot shown in Figure 11d, which was recorded 1.1 ns after the initial application of the field, formation of jets emanating from both ends of the elongated droplet are apparent. Although a large solvated ion (with ~20 formamide ligands) with a single Na^+ ion at the center, is seen to be on the verge of being emitted at the positive end of the parent droplet (on the right in Figure 11d), a large complex negative ion, $I^-(NaI)(HCONH_2)_n$, is seen to be detaching at the other (negative) end of the droplet (left in Figure 11d). About 25 ps after the instant when the configuration shown in Figure 11d was recorded, a section of the material streaming from the positively charged end of the droplet thins down to a narrow hydrogen bonded filament of formamide molecules. This results in the detachment of a cluster, or nanodroplet, of charge +3 (see Figure 11e) consisting of 17 Na^+, 14 I^- and ~200 formamide molecules. This corresponds to a mass-to-charge ratio of about 11.2 kamu (kDaltons).

The charged clusters that detach from both ends of the droplet are accelerated by the applied electric field. Their physical characteristics (charge, mass, size, energies) are recorded when they cross two planes (which we refer to as "detection planes") located at ±200 nm from the droplet center along the field direction (the z-axis). Properties of the recorded positively and negatively charged clusters are summarized in Figure 12 as a function of the cluster radii, R, estimated by using the equimolar radius defined by the cluster mass, m, the computed density of the NaI−formamide solution, $\rho \sim 1.32$ g/cm^3, and the relation $m = 4/3\pi R^3\rho$. Figure 12a displays the estimated surface electric field, E, of each cluster using Coulomb's law (eq 2). A change in the dependence of E on the cluster radius, R, is observed at $R \approx 1$ nm, with clusters having radii $R \leq 1$ nm corresponding to single ions solvated by formamide molecules, whereas clusters with $R \geq 1$ nm are characterized as multi-ion droplets. In the latter, dispersion forces are expected to have a more important contribution in conjunction with electrostatic interactions. The change in behavior occurring for clusters with $R \geq 1$ nm is reflected also in the q/m and q/q_{Rayleigh} ratios plotted in Figure 12b,c, respectively. The arrow on the horizontal axis in Figure 12 corresponds to the experimental estimate (see Table 1 for the 1:8.4 mol ratio) for the radius of curvature of the electrospray jet, $R_{\max}$, at the point of maximal electric field, $E_{\max}$ (see eqs 6 and 7). Essentially, all the clusters recorded in the MD simulation have radii smaller than $R_{\max}$. The few clusters with radii larger than $R_{\max}$ appeared at the very end of the simulation when breakup of the droplet into large fragments was observed. The experimental estimate for $E_{\max} = 1.67$ V/nm (determined from eqs 6 and 7 as the average between the positive and negative polarities) is indicated by the solid line in Figure 12a. The estimated surface field of the simulated clusters remains very close to $E_{\max}$ for cluster radii in the droplet regime.

Figure 12b shows the charge-to-mass ratios for the clusters emitted by the simulated droplet. The mean value of the experimental q/m (Table 1), averaged over polarities, is shown as the horizontal dashed line (near the bottom in Figure 12b). The MD simulation values rapidly approach the mean experimental value as the cluster sizes enter the droplet regime. If one uses $E_{\max}$ as an estimate for the limiting value of the surface field for a charged droplet in eq 2 (Coulomb law) to write $q = 4\pi R^2\varepsilon_0 E_{\max}$, an estimate for the upper bound of q/m can be obtained from

$$q/m = 3\varepsilon_0 E_{max}/\rho R \quad (12)$$

The upper bound for q/m as a function of E_{max} and R is indicated in Figure 12b by a solid line. It is evident that the data for charged droplets ($R > 1$ nm) recorded in the MD simulations follow the predicted trend.

In Figure 12c we display the ratio between the observed (MD) charge and the predicted charge for Rayleigh instability and fission, computed from eq 1, with the surface tension $\gamma = 0.046$ N/m determined from the MD pure formamide droplet. The charge for clusters in the droplet regime exhibits variations about 0.5 of the Rayleigh limit. Using eqs 1 and 2, one obtains the upper limit for the ratio, $q/q_{Rayleigh}$:

$$q/q_{Rayleigh} = (\varepsilon_0 R/4\gamma)^{1/2} E_{max} \quad (13)$$

The corresponding values of eq 13 are shown as a solid line in Figure 12c. This simple estimate captures the general trend and values observed in the MD simulation. As mentioned earlier, the largest droplets were produced at the end of the simulation during the disintegration of the main droplet.

Profiles of ion (Na^+, solid line; I^-, dashed line) and solvent (circles) molecular densities along the semimajor axis of the droplet spheroids for the cases (with $\eta = 1$, 1.5 and 2) shown in Figures 11a–c, are compared in Figure 13. Also included in this figure are profiles of the local electric field (squares for the field outside the droplet and dotted line for the interior field) and the ionic charge density, the latter given by the difference between positive and negative ion densities (see the lower solid line, near the horizontal axis, in each panel). The plotted electric field does not include the external field (0.625 V/nm). The densities are calculated by defining prolate spheroid shells that match the instantaneous droplet shape and end curvatures, and by counting the respective species between neighboring shells and within a 1 nm core radius with respect to the z-axis. Although the radial diameters of the narrowing droplet ends (along the z-axis) are less than that of the sampled core diameter (2 nm), the contributions to the statistics of the density come only from material inside the prolate spheroid shells, thereby yielding an accuracy superior to that obtained via simple binning of the z-axis. This process was not implemented for the case of the droplets in Figures 11d,c due to the narrow, rapidly varying, curvature. The data are obtained from 300 ps time averages in the vicinity of the snapshots shown in Figures 11a–c.

The electric field strength along the z-axis is computed by binning (during the simulation) the number of each species (Na, I, and the six atoms in each formamide molecule, each having their own partial charge) with the z- and r-axis having bin widths of 0.2 nm. The binned data is averaged over a specified time in which the droplet does not change its shape or size significantly. On the basis of the charge of each species, the binned number of atoms provide the average amount of charge coming from each species in each of the radial "rings" associated with each z-bin. The potential $V(Z)$ at a point, Z, on the z-axis is given as a sum of the contributions from the total charge, q_i, in each of the binning rings of radius, r_i, for all the z-bins (except for the central radial bin in the z-bin for which the field is determined):

$$V(Z) = \sum_i \frac{1}{4\pi\varepsilon_0} \frac{q_i}{((z_i - Z)^2 + r_i^2)^{1/2}} \quad (14)$$

The electric field at point Z, originating from the ionic and molecular charges (not including the external field) is then given by $E(Z) = -\partial V(Z)/\partial Z$.

The field-free droplet (Figure 13a) exhibits a depletion of ions at the interface, with a slightly higher ion density in the second or third interfacial layer (~6 Å from the interface) in comparison with the bulk. Differences between Na^+ and I^- densities are insignificant. This is consistent with the traditional view[102] pertaining to the behavior of the interfacial region of salt solutions, and it contrasts with recent MD and experimental findings in aqueous NaI solutions, where the highest I^- densities were found in the outer interfacial layer;[54,55,64,66,67,102] we defer further comments on this issue to our discussion in section 5.

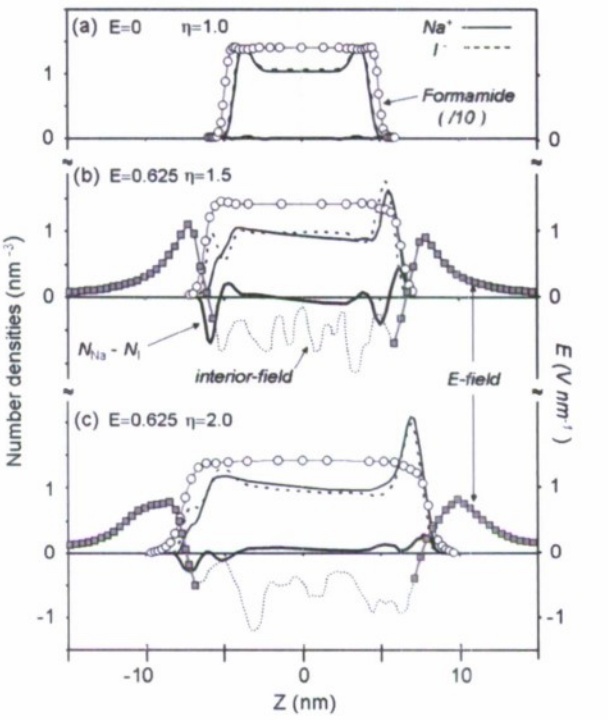

Figure 13. Number densities and induced electric field of the 1:16 ratio NaI–formamide droplet along the field direction for (a) no external field, (b) elongating in an applied (external) field of 0.625 V/nm, before emitting ions, and (c) during the time of initial cluster-ion emissions. The profiles correspond to the respective snapshots in Figure 11a–c. The number density profiles of the droplet components (Na^+, I^-, and formamide) are shown in (a)–(c), with line designation given in (a). In (b) and (c) we show also the difference in number densities of the ions $N_{Na} - N_I$ (solid line near the axis; see designation in (b)), as well as the electric fields. The internal field of the droplet (generated by induced surface charges) is shown as lighter lines and fluctuates around ~−0.6 V/nm. The induced field outside the droplet is given by squares (connected by a line, marked E-field). The aspect ratios, η, for the various configurations are specified in the figure.

In Figure 13b we display the density profiles for the droplet shown in Figure 11b. The interfacial charge density has clearly increased compared to the $E = 0$ case (Figure 13a). Near the positive end (right in Figure 13b), there is a slight preference for positive ions with ion densities of both polarities peaked at the interfacial layer. At the negative droplet end, there is a clear preference for negative ions in the interfacial layer. The droplet electric field strength (due to the droplet charges) is highest outside the droplet (beyond the droplet ends) with total fields (including the applied field) exceeding 1.5 V/nm. Interestingly, the maxima are displaced away from the maxima in the ion density, suggesting that the aligned dipoles of the solvent molecules contribute considerably to the electric field in the immediate vicinity of the ends of the droplet. Indeed, when the field produced by the droplets is decomposed into contributions from the ions and the formamide molecules, we find that both make significant contributions. It is also of interest to note that the axial electric field of the pure formamide droplet (placed in

an external field of 0.5 V/nm; see Figure 10) is essentially the same as that shown in Figure 13b for the salt solution droplet. In the pure formamide droplet the total contribution to the droplet polarization field comes from the aligned dipoles of the formamide molecules. From the fact that the fields in the exterior of the droplet have similar magnitudes in the pure and salt solutions droplets (where in the latter both the molecular diploes and the dissolved salt ions contribute to the total field), we conclude that the larger contribution of the molecular dipoles in establishing the field in the salt-free formamide droplet reflects a higher degree of dipole alignment in such droplets compared to that in the salt solution ones where the dissolved ions frustrate the molecular alignment along the field direction. Direct analysis of the dipole alignments in pure formamide and salt solution droplets verifies the above conclusion. We also note that the field strengths (of the order of 1 V/nm) originating from droplet polarization, are established very shortly after application of the external field and before the occurrence of any significant field-induced elongation.

The field produced by the charges of the constituents of the droplet vanishes asymptotically far from the droplet, so that the total summed field converges to the external constant field of 0.625 V/nm. The negative field inside the droplet is of the same nature as the field within a dielectric slab or sphere subjected to an external field (see dotted line in Figure 13b,c). Charges of opposite polarity are induced on opposing sides of the dielectric and this creates an internal field that opposes the external field.

In the present case, the average internally induced field is ~ -0.58 V/nm, corresponding to a small total internal field, $E = 0.625 - 0.58 \sim 0.04$ V/nm. Such small internal fields are typical of dielectric materials responding to external electric fields. The high sensitivity of computed dielectric properties to small variations in this internal field necessitates the accumulation of sufficient data that would permit a meaningful statistical analysis. The highly oscillatory nature of the field within the drop seen in our simulations is due to limited statistics and the fact that the computed field reflects a nonuniformity of the ionic distribution that does not self-average over the averaging interval of ~300 ps used in these simulations.

4.3.3. Charge Emission Statistics. Statistics on charge emission is collected during the simulation by recording the passage of all ejected clusters through the aforementioned "detection planes" placed at ±200 nm along the z-axis. The atomic position and momentum data of each cluster are also recorded so that the evolution of each individual cluster can be examined in a separate continued simulation of the isolated species (after the given cluster is essentially free from all the others).

The surface tension of the NaI−formamide droplets is comparable to that of the pure formamide droplet and the predicted critical field for instability[17] discussed earlier (see also Figure 10) is similar. However, in the salt-solution case, the droplet does not simply elongate to another stable configuration at the critical field. Instead, the imbalance between electrical stresses and capillary forces is relieved through a more favorable route, namely one involving formation of a jet of charged clusters (at each end of the elongated nanodroplet). At the smaller investigated fields (<1 V/nm), the droplets elongate more slowly and emit cluster ions less frequently with the result that capillary, Rayleigh-type, instabilities lead to break-up of the droplet into large charged segments that are accelerated out of the computational cell before the number of cluster ions that are emitted is adequate for meaningful statistics. Consequently, when investigating cluster-ion emission statistics, we focus on

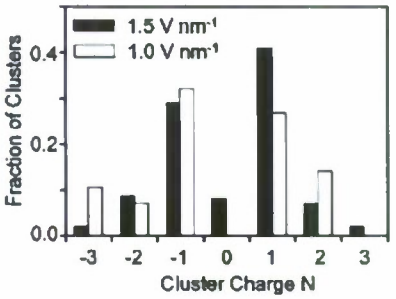

Figure 14. Charge abundances of ion-containing clusters emitted from a 1:8 ratio NaI−formamide droplet placed in a uniform external field. Results are shown for external field strengths of 1.0 and 1.5 V/nm.

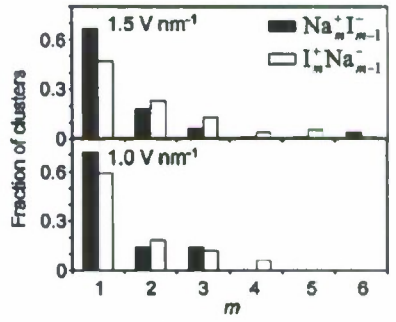

Figure 15. Ion composition of singly charged formamide/NaI clusters emitted from a 1:8 ratio NaI−formamide droplet placed in a uniform external field of 1.5 V/nm (top) and 1.0 V/nm (bottom).

simulations of droplets at the higher field strengths. The improved statistics associated with the higher charge fluxes allows for a better comparison with the mass spectrometric measurements.

Under the influence of an electric field of 1.5 V/nm, the droplet begins to deform along the axial field direction about 10−20 ps prior to charge emission of positively and negatively charged solvated ions from opposite ends of the drop. Over the course of about 1 ns, the parent droplet continues to elongate to at most an aspect ratio of $\eta = 8$, and the onset of charge emission is observed. The continuous stream of charged particles prevents elongation to higher aspect ratios such as the one observed for the pure formamide droplet (see Figure 10). The simulations demonstrate that charge emission happens from multiple sites on each end of the drop. This is consistent with a stressed, multicone electrospray regime discussed earlier. We remark here that, because of the early emission of charged particles in simulations employing a high electric field (1.5 V/nm), most of our analysis focused on lower applied fields which enable an improved comparison with the experiments, particularly on issues pertaining to the dynamics of the cluster ion emission and droplet formation.

The charge distribution of cluster ions originating from formamide droplets containing 29% (by weight corresponding to 1:8 mol ratio) of dissolved NaI is shown in Figure 14. Results are presented here for two separate simulations having externally applied electric field strengths of 1.0 and 1.5 V/nm. The abundances of charge in both of these simulations are similar, showing that the majority of the observed clusters have ± 1 charge.

More detailed information on the ionic composition of the most frequently observed clusters of charge ±1 is shown in Figure 15. In the case of positive singly charged clusters, the fraction of clusters with ionic composition Na^+, $Na_2{}^+I^-$, etc and for negatively charged clusters, the fraction corresponding

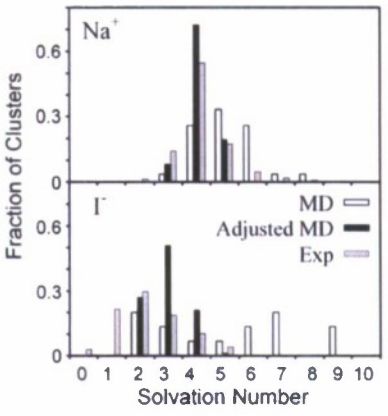

Figure 16. Solvation number distribution of single-ion clusters emitted from a 1:8 ratio NaI−formamide droplet under a uniform external field of 1.5 V/nm. MD results corrected for 30 μs flight time (adjusted MD) are also shown (see text for details).

to I^-, $Na^+I_2^-$, etc, are shown regardless of the number of accompanying adsorbed (solvating) formamide molecules. Though multi-ion clusters are formed, the primary contribution is from single-ion clusters (Na^+ and I^- with varying numbers of adsorbed formamide molecules). Furthermore, the multi-ion cluster fraction increases with field. This is consistent with the present experimental single cone-jet observations at lower representative field strengths, where the multi-ion fraction due to $Na_2^+I^-$ and $Na^+I_2^-$ solvated ions, is very small (see Figures 4 and 5).

In Figure 16 we compare the solvation number distribution of the single-ion positive and negative cluster ions compiled from the concentrated (1:8 mol ratio), 1.5 V/nm MD simulation to those observed in the concentrated electrospray experiment. Also shown are MD results adjusted for a ~30 μs flight time using the calculated survival fractions from Tables 3 and 4 for 300 K. For Na^+ and I^- solvation numbers exceeding 6 and 5, respectively, a zero survival fraction is assumed, but for $n < 4$ and 3, respectively, a 100% survival is implied. The Na^+ clusters have predominantly 4−5 formamides, and the adjusted cluster distribution compares well with the experimental abundances. The I^- clusters exhibit a much broader distribution with some preference toward lower solvation numbers. The adjusted MD statistics are again consistent with the experimental results (Figures 4 and 5) for a single cone-jet electrospray of the same concentrated solution.

5. Discussion

The close correspondence that we found between the data measured in the vacuum electrospray experiments and the results recorded in our theoretical MD simulations performed on liquid drops (made of pure formamide or NaI−formamide solutions) demonstrates that such coordinated, complementary, and supplementary studies form a most valuable methodology, and an invaluable source of information and deep insights pertaining to the complex physics and operational control of electrosprays, nanojets, and charged droplets under the influence of high electric fields. Having presented in the previous sections our laboratory measurements and theoretical simulations, we discuss now certain issues that have emerged through the analysis of the results of our investigations.

The characteristic parameters of our experiments (see Table 1) demonstrate that the cone-jet generated in these experiments operates in the nanoscale jet regime with sufficiently high fields generated normal to the liquid surface to induce effective field evaporation of ions. The observed average mass-to-charge ratios and the significant cluster-ion currents are signatures of a mixed droplet/ion emission regime where a significant amount of current is produced by ion field evaporation from the cone-jet surface, whereas the mass flow is dominated by the droplets. Although pure ion emission would result in average mass-to-charge ratios below 1000 amu, typical mixed droplet/ion emission with weak ("background") ion currents, possibly due to droplet ion emission, yields average mass-to-charge ratios near and above[47] 10000. The present average mass-to-charge ratios, which are below 10000 (but well over 1000), point to an intermediate regime with comparable contributions from ions and charged droplet currents. This conclusion is further consistent with the estimated values for the maximum surface-normal fields, E_{max} (between 1.4 and 1.7 V/nm), and for the critical radii, R_{max} (between 2 and 3 nm), derived from the axial emission currents and mass flows, thus confirming predictions obtained from the theory of cone-jet emission.[34−41] The deduced jet diameter of about 5 nm is comparable to that of the simulated droplets, supporting the comparison between the present electrospray experiment and the MD simulations.

Decreasing the salt concentration of the NaI−formamide solution leads to a reduction of the maximum surface-normal field strength and an increase of the associated radius of curvature. This is consistent with eqs 6 and 7. The expected increase in m/q, however, is found to be significant only for negatively charged emitted particles. This somewhat surprising result can be explained by the substantial decrease in charged particle beam divergence upon dilution, as reflected by the ratio of the Faraday Cup current with respect to the total emitted current. As angular distribution measurements on ionic liquid cone-jets operated in a nano regime have shown,[51,52] the m/q distribution can be nonuniform with respect to the emission polar angle. Thus, the derived average m/q value is only representative of charge emission captured at small angles with respect to the capillary axis. The nonuniformity reported by Chiu et al. for the ionic liquid, [Emim][Im],[51,52] is consistent with predictions that the surface electric field is highest at the cone-jet neck, where field-evaporated ions are driven away from the cone-jet axis.[41,43] The respective field-evaporated ions are, therefore, preferably emitted at large angles whereas droplets, emitted from the jet tip, have narrow angular distributions centered on axis. This interpretation was further confirmed for the ionic liquid by the measured energy distributions demonstrating that the ions peak at energies nearly equal to the emitter potential, whereas the droplets appear at lower potentials. Consequently, if similar field evaporation dynamics is operative in the present concentrated NaI−formamide solution, a significant fraction of the ion current is not detected by the Faraday Cup, and the average value of m/q for the entire jet is considerably higher for cases with substantial divergence of the ionic component in comparison with the droplet component. This interpretation, however, is contradicted by the fact that the present retardation potential measurements (Figure 7) show that only a small fraction of ions are produced at energies exceeding the droplet energy, suggesting that most ions are formed in a region of the neck downstream from where ohmic losses have occurred. Similar retarding potential results have been derived by Gamero-Castaño for concentrated NaI−formamide at low flow rates.[43] Consequently, the field evaporation dynamics of the present solution may not be equivalent to that observed for the ionic liquid [Emim][Im]. This does not discount the possibility that ion emission is more divergent than the droplet spray.

In addition to field evaporation from the jet, ions can he emitted from droplets as described by the mechanism of Iribarne and Thomson[24] for electrosprays of volatile solvents in an ambient atmosphere. This requires that the surface electric field strength, given by eq 2, exceeds the ion evaporation (desorption) limit. However, this mechanism can only lead to a current that is a small fraction of the total droplet current because the surface-normal field strength is expected to decline below the field evaporation limit following the emission of only a few ions,[41] particularly for nonvolatile droplets of nanometer dimension.

Further insights were obtained here through comparative mass spectrometric studies of concentrated and dilute NaI−formamide solutions. Although the distribution of Na^+ solvated ions is very similar at the two concentrations, apart from a greater number of trace ions at high solvation numbers, the I^- solvated ion distribution broadens considerably and shifts to higher solvation numbers upon dilution. This behavior is consistent with recent theoretical and experimental investigations of aqueous salt solutions,[53−57,60−67,102] where the observed preference at the interface for more polarizable anions such as I^- was explained and correlated, in part, with the broader range of solvation numbers that the anion can accommodate, in comparison with less polarizable anions and cations, which prefer more rigid, hydrogen-bonded, solvation shells. Thus, as the concentration decreases, more solvent molecules are available to bond with I^-, whereas Na^+ maintains a tightly bound structured solvation shell.

The fraction of Na^+ ions with solvation number $n > 4$ drops rapidly. Indeed, for such solvated clusters room temperature thermal instability is predicted; the present quantum chemical results (see Table 2) predict that the solvated ions become thermally unstable at room temperature above $n = 4$. The I^- solvated clusters are predicted to be thermally unstable for $n > 3$. Results from ab initio calculations provide a lower bound for the largest value of n that provides a stable cluster at room temperature. The calculations assume that all the energy that is available to the system is channeled into a dissociative mode. However, deviations from the observed experimental values of n suggest that the energy is distributed among several available modes whose number increases with n. Overall, the ab initio and RRKM calculations do not preclude the existence of I^- solvated cluster with $n > 3$. In fact, the larger number of ions with high, thermally unstable, solvation numbers observed upon dilution, suggests that a significant number of cluster ions are emitted with large, unstable, solvation numbers, which subsequently lose (via evaporation) solvating ligands, resulting in evaporative cooling of the product cluster ions. This effect is even more pronounced for the I^- cluster ions, to the point that the most abundant solvation number lies beyond the present predictions of thermal stability at a liquid temperature of 298 K (Table 2).

Similar behavior was observed in our experiments on KI solutions, where the K^+ solvated ions also have maximum abundances near the predicted limit of thermal stability. The main difference between the KI and NaI solutions are the survival of complex ions (of both polarities) upon dilution for both ion polarities, observed for the KI case. The KI experiments were mired by crystallization of the solute and, therefore, had to be conducted at significantly lower molar concentrations. The higher propensity for forming complex ions $[X^{\pm}(KI)(HCONH_2)_n$, $X = K^+$ or $I^-]$, despite the lower concentration in comparison with the NaI solution, may be a manifestation of the lower solubility of the KI solute.

The snapshots of the droplet configurations recorded in the simulation of a NaI−formamide solution droplet with 1:16 (NaI−formamide) ratio (Figure 11) under the influence of an electric field of 0.625 V/nm, reveal a number of features that are in direct correspondence with the experimental observations. In particular, in both cases we observe mixed droplet formation and field-induced ion evaporation (desorption) events. Formation of nanojets is clearly observed in the simulations (see Figure 11d where a jet with a diameter of about 2 nm is shown). However, we remark that the jet emerging in our simulation is a transient state whose further development prior to particle emission and breakup into droplets may be limited by the finite size of the simulated drop. In the experiment, on the other hand, a continuous (unlimited) source of liquid is present, thus allowing the development of steady-state jet (flow) conditions. Therefore, to allow a detailed theoretical study of the breakup processes, simulations at lower applied fields were favorable. Interestingly, in the simulations, the majority of cluster ions are found to be emitted from the tip of the jet rather than from the neck region next to the Taylor cone (for geometrical definitions see Figures 1 and 2). This finding is consistent with the experimental energy distributions of the solvated ions, which demonstrate that indeed most ions are emitted closer to the jet region, that is, beyond the cone-neck region where ohmic losses occur. This observation is also consistent with continuum electrohydrodynamic predictions of cluster-ion evaporation at surface regions of high curvature and therefore maximum surface electric field strengths, which may he the cone-neck region, the breakup region of the jet (usually near the tip of the jet), or the emitted charged droplets.[41,43] In the nanoscale jets observed in this study, the regions of highest spatial curvature are at the ends of the jets where nascent drops are either forming or have just detached.

Because of the small dimensions of the jets formed in the MD simulations, as well as deduced from analysis of the experimental measurements, one may indeed expect that a continuum approach would fail to provide an adequate description of the evolution and breakup processes of the complex liquid system on which we focus here. From inspection of the droplet configurations displayed in Figure 11, we observe the occurrence of spatial and temporal fluctuations of the ion density that are expected to influence in a significant manner the electric field distribution and the consequent stability and evaporation/fragmetation dynamics of the system. Indeed, we have noted that droplet formation events (location and timing) correlate with instances of ion bunching in the jet region. These observations are likely to be of particular relevance to electrolyte solutions where bunching of the solute ions (sodium and iodine ions in our case) occurs; indeed, in the case of an ionic liquid (where ions are distributed uniformly, unlike our case here of salt solutions where the solute salt ions are dissolved in a polar solvent), certain characteristics that indicate emission from the neck region have been observed,[51,52] even though the jet diameter in that system is estimated to be similar to that found in the present study. Additionally, stochastic thermal effects play a much increased role for fluid jets of nanoscale dimensions,[69] modifying the kinetics of fluid pinch-off from the predictions of a purely deterministic continuum approach. Formulation of electrohydrodynamic theoretical treatments of instabilities and fragmentation, with the inclusion of fluctuations due to inhomogeneities in the solvated ionic charge distribution in the fluid as well as size-dependent thermal noise, present a formidable future challenge.

An important prediction obtained from the MD simulations concerns a crossover behavior as a function of the size of the emitted species, which distinguishes between two distict regimes: one corresponding to solvated single-ion clusters with radii $R \leq 1$ nm, and the second one corresponding to multi-ion droplets that emerge for larger size fragments, $R > 1$ nm. Such crossover is indeed found experimentally, and it may be explained through electrostatic considerations (see Figure 12). This crossover reflects stronger bonding in the smaller, single-ion solvated clusters due to direct ion-dipole interactions which correlate with the ability to sustain larger values of charge-to-mass ratios compared to larger size clusters (see Figure 12b).

Emission of clusters that include ion pairs was detected in both the experiments and the simulations. Though only species containing a single ion pair were observed in the experiments for concentrated NaI formamide solutions, and none for the dilute solution, higher fractions of such ions with species containing two or more ion pairs were found in the simulation (Figure 15). Note that the respective radii of the complex ions containing ion-pairs exceed 1 nm, and exhibit electrostatic properties of droplets according to the analysis of Figure 12. We have not conducted an RRKM analysis and thermochemical analysis for these species to assess whether such complex ions decay faster than the experimental time scale. Similarly, no multiply charged ions were detected in the experiments, although they were found in the simulation (Figure 14). Higher field strengths do not appear to be the source of these findings because an increase of the field in the simulations from 1 to 1.5 V/nm did not affect the observed trends (see Figures 14 and 15). We note, however, that earlier vacuum electrospray studies conducted with glycerol solutions observed a multitude of solvated ions including metastable ions and multiply charged species.[3,31,32,103]

In general, the emitted cluster ions recorded in the MD simulations contain more nascent formamide molecules (that is, they are characterized by larger solvation numbers) than the clusters observed in the experiments where typical flight times (that is, the elapsed time between the instant of cluster generation and the moment of its detection) are of the order of 30 μs. The recorded occurrence of larger solvated ion clusters is likely to be correlated with the propensity of the solvent (formamide) to form hydrogen bonds (see Figures 11c−e). Because the largest solvated ions observed in the MD simulation are thermally unstable, evaporative loss of formamide molecules over longer flight times can effectively lower the average solvation numbers to values close to those found experimentally (see Figure 16). The observation of larger solvated ions in the simulations suggests that such larger cluster ions are indeed generated in the laboratory experiment, and that subsequently these large, thermally (room temperature) unstable clusters reduce their size via a cascade of evaporative cooling processes that occur along the ion trajectories to the detector. Indeed, separate simulations on large thermally unstable cluster ions show that the loss of a formamide molecule leads to an approximate reduction of about 50 K in the cluster-ion temperature. As evident from the data shown in Table 3, a 50 K change in temperature has a rather significant effect on the stability of the cluster ions.

Although the comparison with the present experimental solvated Na^+ ion distributions, predicted thermal stabilities, and RRKM decay rates suggest a surface temperature below 350 K, a 200 V drop between the capillary potential and the observed ion appearance potential indicates the occurrence of ohmic heating in the neck region of the cone-jet. Thus, a slightly elevated temperature at the point of ion field evaporation could be expected. We also note here that in the MD simulations we observed an increase in the nascent cluster-ion temperature from 310 K to about 400 K from the beginning to the end of the simulation. This can be attributed to the fact that the simulations were conducted at a relatively high external field, corresponding to stressed conditions.

A rather convincing illustration that the emitted charged droplets recorded in the simulations are consistent with the values deduced from the experimental data for the characteristic maximal electric field, E_{max}, and the corresponding local curvature (determined by the local radius, R_{max}, of the flowing fluid structure), can be found in Figure 12. We find that the surface fields of the droplets are close to the experimental, polarity averaged, value of E_{max}, which is found to be close in value to the interfacial field determined from the simulations (see Figures 12a and 13b,c). Additionally, the charge-to-mass ratio associated with the experimental maximal value of the electric field, E_{max} (eq 12), is found to agree well with the values derived for the emitted charged droplets (see Figure 12h). Finally, the observed trend in the emitted droplet charge (as a fraction of the predicted Rayleigh limit) is found to be consistent with the upper limit given by eq 13 when using the experimental value of E_{max} (see Figure 12c).

It is pertinent to remark here on the small asymmetry between the calculated negative and positive ion interfacial density profiles (see Figure 13), particularly in light of recent interest in the interfacial properties of aqueous solutions.[53−67,102] Upon application of an electric field, the ion density at the interface increases (see Figure 13b). At field-free conditions no discernible difference is found between the negative and positive ion interfacial densities. However, when the simulated droplet is placed in a uniform electric field, it exhibits a preference for negative ions to be found near the negative polarity interface, whereas positive ions are preferred at the positive end. The derived solution-induced electric field strength normal to the surface at the negative end exceeds 1.0 V/nm, corresponding to a total field strength of about 1.6 V/nm when including the external field. This value is again in excellent agreement with the derived values for the concentrated solution (see value in Table 1, obtained with the use of eq 6). The field is slightly lower at the positive end. The large surface fields at the polar ends of the drop are not solely a reflection of the ionic charge density but are attributable to both aligned formamide dipoles as well as field-induced polarization and separation of the ionic charges. Similar surface fields are deduced for the pure formamide droplet (see Figure 10) where, as noted above, the lack of ionic charge is compensated by an increased field due to a higher formamide dipole-field alignment. As aforementioned, the above indicates that in solution droplets the presence of solvated ions frustrates the alignment of the dipolar solvent molecules. We conclude that the contribution of the solvent (particularly molecular orientational polarization) to the interfacial field must be included in a proper description of the dynamics of electrosprays (emanating from from jets or droplets) of salt solutions, particularly for systems of nanoscale dimensions (as well as in discussion of the microscopic aspects of larger ones). Closer inspection of the molecular configurations in the neck region (see, e.g., Figure 11) reveals that the dipoles of the interfacial solvent molecules near the neck are aligned by the field more in the direction of the flow than normal to the surface. Consequently, the field evaporation force normal to the surface is reduced, thereby providing an explanation for the lack of ion emission at the neck.

The observed preference of negative ions at the interface, under the influence of an external electric field, is not as pronounced as the corresponding findings at aqueous interfaces under field-free conditions, where large polarizable anions were particularly preferred over cations in the interface layer.[54,55] From the fact that the simulated field-free NaI−formamide droplet exhibits no difference between anionic and cationic densities in the interface layer (where ion depletion occurs as expected from a solvation energy consideration), we conclude that the minor preference for the anions to reside in the interfacial layer, found in simulations under the effect of an external field, is related to the interaction of the ions in the cluster with the applied field. Because the solvation number distributions are broader for the larger anions, and because the ligand binding energies are weaker (see Table 2), it may be expected that the propensity of the formamide molecules coordinated with the I^- to align with the field is higher than that of molecules coordinated with the Na^+ cations, resulting in a stronger attraction toward the high-field region at the interface.

Additionally, the lack of charge preference in the field-free NaI−formamide droplet could also be attributed to the nanometer-scale droplet confinement effects, surface curvature, and characteristics of the liquid solvent (that is, formamide in the present simulations versus water in previous interfacial studies). The chemical identity factor could be of principal significance, particularly in light of the fact that the behavior of aqueous solutions is often discussed in terms of hydrogen bonding between water molecules in clusters of large anions, versus symmetric solvation in the case of the cationic systems.[102] Accordingly, it has been shown through MD simulations of aqueous Na^+ and Cl^- clusters, that Na^+ is solvated symmetrically in the center of the clusters, and Cl^- resides on the surface of a water cluster.[104] This was confirmed experimentally for the larger halide ions in water dimer clusters by Johnson and co-workers.[105] The present ab initio optimized structures of formamide-solvated ions, however, show no evidence for hydrogen bonding with both the formamide-solvated Na^+ and I^- ions located close to the centers of the corresponding clusters. This comparison calls for similar simulations of electrospray dynamics in solutions with volatile solvents such as those used in mass spectrometric electrospray experiments involving an electrospray source operating at atmospheric pressures. The general jet dynamics described in the present work are applicable to volatile solvents in an atmospheric source. The present work, however, demonstrates that irrespective of solvent volatility and gas-phase pressure, the detailed field-evaporation dynamics need to be examined on a case-by-case basis because they are governed by complex solvation dynamics at the liquid−air interface and its response to electric fields with strengths on the order of 1 V/nm. We remark here that to perform MD simulations on aqueous drops would require the inclusion of a gaseous atmosphere, which constitutes an added complexity in the simulation. Additionally, comparisons with experimental data on nascent ion distributions, enabled here (in part) by the low-vapor pressure of the solvent (formamide), are not available for aqueous solutions.

6. Summary

In this paper we presented laboratory experiments and theoretical investigations aiming at characterizing and understanding the atomic-scale structure, energetics, stability, dynamics, and fragmentation processes of complex liquids under the influence of high electric fields. The present MD simulations of drops of NaI−formamide solutions placed in a uniform field reproduce faithfully the main salient experimental features observed in vacuum electrospray ionization experiments of solutions of similar concentration, operated in a single cone-jet mode with jet dimensions comparable to the drop size. At these conditions, Taylor cones spray charged particles in a mixed solvated ion/droplet regime. The MD simulation of a droplet subjected to a uniform electric field of 0.625 V/nm shows the occurrence of droplet fission and field ion evaporation processes. The simulation predicts that ion emission occurs at the breakup region of jets (see Figures 2 and 11d,e) where nascent charged droplets form and get emitted, as well as at the tips of elongated charged droplets and the nanojets that emanate from them. This is consistent with studies that correlate enhanced cluster-ion emission with the regions of highest spatial curvature.[41,43] The results from the simulation are consistent with the present experimental findings that most of the field evaporated ions are formed with energies near, or lower, than those of the charged droplets. The surface normal field strength determined from the simulation near the point of charge emission (for the concentrated solution droplet) is determined to be ~1.6 V/nm, in excellent agreement with the field derived from the experimental observations using continuum electrostatic theory. The size dependence of the surface electric field and charge-to-mass ratios of droplets emitted in the MD simulation are fully consistent with the experimentally derived maximum surface field strength and associated curvature. A transition in the electrostatic properties of the emitted clusters as a function of size is observed at radii of ~1 nm, corresponding to a transition between solvated single ions (for $R \leq 1$nm) and multi-ion droplets (for $R > 1$nm). This crossover is attributed to the stronger intermolecular forces and the consequently higher sustainable charge densities in the solvated single ions.

The simulated and measured solvation number distributions for $Na^+(HCONH_2)_n$ and $I^-(HCONH_2)_n$ are in good agreement. Though the Na^+ cluster-ion distributions are governed primarily by thermal stability and are independent of concentration, the I^- cluster-ion distributions broaden with dilution. Similar behavior is observed experimentally with KI−formamide solutions. Larger cluster ions that are thermally unstable at 300 K are observed and attributed to evaporatively cooled species. Complex ions including ion pairs are observed both in experiments and in the simulations. Although multiply charged ions are not observed experimentally, minor quantities of multiply charged ions survive the ~15 ps flight time of the simulation space.

The present MD simulations reveal that for a NaI−formamide droplet at field-free conditions, ion densities are depleted in the interfacial region and that there is no preference of anions over cations (see Figure 13a). Application of a field polarizes the droplet through molecular dipole alignment and ion charge redistribution resulting in excess positive charge (and cation concentration) and excess negative charge (and anion concentration) at the opposing ends of the droplet. The resulting electric field strength at the exterior surface of the droplet is due to both the molecular dipole alignment and polarized ion distribution and is of a magnitude 1 V/nm (leading to a total electric field of ~1.5 V/nm when the externally applied field is added).

In summary, the combined theoretical and experimental investigations presented in this paper provide deep insights pertaining to the microscopic origins of the properties of charged dielectric fluids (that is, salt solutions of formamide) with (and

without) the influence of externally applied electric fields. In particular, these studies have unveiled certain molecular-scale aspects of the instabilities and mechanisms leading to breakup and fragmentation of liquid structures. These studies allow us, in addition, to assess the validity of continuum hydrodynamic and electrohydrodynamic theories for the description of charged fluids of nanosale dimensions, and they may serve as a guide for the testing and development of improved treatments, such as the stochastic hydrodynamic formulation formulated and applied recently in studies of liquid neutral nanojets and nanobridges.[69,70]

Acknowledgment. We acknowledge support by the Air Force Office of Scientific Research as part of the Space Miniaturization Theme and under task 2303ES02 (Program Manager. Michael R. Berman), and in part by a grant from the Department of Energy (to UL). The molecular dynamics simulations were performed at the Georgia Institute of Technology Center for Computational Materials Science and at the National Energy Research Scientific Computing Center (NERSC), Berkeley, California, through a grant to U.L. Y.C. acknowledges the grants of computer time from the Maui High Performance Computing Center and DoD High Performance Computing Center at the Aeronautical Systems Center site. S.S. acknowledges Dr. Srinivas Aluru for providing access to the IBM BlueGene/L supercomputer (CyBlue) at Iowa State University.

TABLE A1: B3LYP/6-31G(d) Predicted Geometries of $Na(HCONH_2)_n^+$, $n = 1-4$[a]

	$Na(HCONH_2)_n^+$			
parameter	$n = 1$	$n = 2$	$n = 3$	$n = 4$
R(O1−C1)	1.248	1.244	1.232	1.228
R(C1−H1)	1.097	1.098	1.101	1.103
R(C1−N1)	1.331	1.334	1.34	1.344
R(N1−H2)	1.012	1.012	1.011	1.01
R(N1−H3)	1.014	1.014	1.013	1.012
R(O2−C2)		1.244	1.232	1.228
R(C2−H4)		1.098	1.101	1.103
R(C2−N2)		1.334	1.34	1.344
R(N2−H5)		1.012	1.011	1.01
R(N2−H6)		1.014	1.013	1.012
R(O3−C3)			1.232	1.228
R(C3−H7)			1.101	1.103
R(C3−N3)			1.34	1.344
R(N3−H8)			1.011	1.012
R(N3−H9)			1.013	1.01
R(O4−C4)				1.228
R(C4−H10)				1.103
R(C4−N4)				1.344
R(N4−H11)				1.012
R(N4−H12)				1.01
α(O1−C1−H1)	121.3	121.5	121.8	122
α(O1−C1−N1)	124	124.1	124.5	124.6
α(H1−C1−N1)	114.6	114.4	113.7	113.4
α(C1−N1−H2)	121.2	121.3	121.4	121.5
α(C1−N1−H3)	120.3	120.1	120.1	119.9
α(H2−N1−H3)	118.5	118.6	118.5	118.7
α(O2−C2−H4)		121.5	121.8	122.1
α(O2−C2−N2)		124.1	124.5	124.6
α(H4−C2−N2)		114.4	113.7	113.4
α(C2−N2−H5)		121.3	121.4	121.5
α(C2−N2−H6)		120.1	120.1	119.9
α(H5−N2−H6)		118.6	118.5	118.6
α(O3−C3−H7)			121.8	122.1
α(O3−C3−N3)			124.5	124.5
α(H7−C3−N3)			113.7	113.4
α(C3−N3−H8)			121.4	119.8
α(C3−N3−H9)			120.1	121.5
α(H8−N3−H9)			118.5	118.7
α(O4−C4−H10)				122.1
α(O4−C4−N4)				124.5
α(H10−C4−N4)				113.4
α(C4−N4−H11)				119.8
α(C4−N4−H12)				121.5
α(H11−N4−25)				118.7

[a] Bond lengths in angstroms; bond angles in degrees. Refer to Figure 8a−d for the atomic numbering scheme.

TABLE A2: MP2/6-311+G(d,p) Predicted Geometries of $I(HCONH_2)_n^-$, $n = 1-5$[a]

	$I(HCONH_2)_n^-$				
parameter	$n = 1$	$n = 2$	$n = 3$	$n = 4$	$n = 5$
R(O1−C1)	1.23	1.228	1.227	1.225	1.222
R(N1−C1)	1.349	1.35	1.353	1.355	1.362
R(N1−H2)	1.028	1.022	1.02	1.018	1.018
R(N1−H3)	1.01	1.011	1.01	1.01	1.011
R(C1−H1)	1.103	1.104	1.103	1.104	1.104
R(O2−C2)		1.227	1.227	1.225	1.224
R(N2−C2)		1.355	1.353	1.354	1.356
R(N2−H5)		1.025	1.02	1.017	1.015
R(N2−H6)		1.011	1.01	1.011	1.011
R(C2−H4)		1.103	1.104	1.105	1.105
R(O3−C3)			1.227	1.225	1.223
R(N3−C3)			1.353	1.355	1.354
R(N3−H8)			1.02	1.018	1.011
R(N3−H9)			1.01	1.01	1.012
R(C3−H7)			1.103	1.104	1.106
R(O4−C4)				1.224	1.221
R(N4−C4)				1.361	1.368
R(N4−H11)				1.02	1.021
R(N4−H12)				1.011	1.012
R(C4−H10)				1.104	1.103
R(O5−C5)					1.224
R(N5−C5)					1.356
R(N5−H14)					1.017
R(N5−H15)					1.01
R(C5−H13)					1.104
α(O1−C1−N1)	126	126	125.7	125.5	125.4
α(O1−C1−H1)	121.9	121.9	122.2	122.3	122.5
α(C1−N1−H2)	120.1	120.1	120.1	119.8	118.5
α(C1−N1−H3)	117.3	118.5	117.6	117.4	116.9
α(N1−C1−H1)	112.1	112.1	112.1	112.2	112.1
α(H2−N1−H3)	118.2	117.7	118.5	118.3	117.9
α(O2−C2−N2)		125.7	125.7	125.8	125.6
α(O2−C2−H4)		122.2	122.2	122.1	122.1
α(C2−N2−H5)		119.1	120	119.9	119.8
α(C2−N2−H6)		117	117.6	118.6	118.5
α(N2−C2−H4)		112.1	112.1	112.1	112.2
α(H5−N2−H6)		117.9	118.5	117.5	117.3
α(O3−C3−N3)			125.7	125.6	125.9
α(O3−C3−H7)			122.2	122.2	122
α(C3−N3−H8)			120	119.9	120.2
α(C3−N3−H9)			117.5	117.6	120.3
α(N3−C3−H7)			112.1	112.2	112.1
α(H8−N3−H9)			118.4	118.4	117
α(O4−C4−N4)				125.4	125.1
α(O4−C4−H10)				122.4	122.6
α(C4−N4−H11)				118.8	117.8
α(C4−N4−H12)				116.9	115.8
α(N4−C4−H10)				112.2	112.2
α(H11−N4−H12)				117.8	117
α(O5−C5−N5)					125.5
α(O5−C5−H13)					122.3
α(C5−N5−H14)					119.6
α(C5−N5−H15)					117.6
α(N5−C5−H13)					112.1
α(H14−N5−H15)					118.5

[a] Bond lengths in angstroms; bond angles in degrees. Refer to Figure 9a−e for the atomic numbering scheme.

Appendix

In this Appendix (Tables A1 and A2) we give the geometrical parameters of the theoretically optimized structures, calculated for clusters of salt ions solvated by formamide molecules.

References and Notes

(1) Fenn, J. B.; Mann, M.; Meng, C. K.; Wong, S. F.; Whitehouse, C. M. *Science* **1989**, *246*, 64.

(2) Fenn, J. B. *Angew. Chem., Int. Ed.* **2003**, *42*, 3871.

(3) Huberman, M. N.; Rosen, S. G. *J. Spacecraft* **1974**, *11*, 475.

(4) Kenyon, R. W. *Chemistry and Technology of Printing and Imaging Systems*; Gregory, P., Ed.; Springer: London, 1996; p 113.

(5) Reneker, D. H.; Chun, I. *Nanotechnology* **1996**, *7*, 216.

(6) Nollet, A. *Recherches Sur les Causes Particulieres des Phénomenes Électrique*; chez les frères Guérin, Rue S. Jacques, A. S. Thomas d'Aquin, Paris, 1749. .

(7) Magnus, G. *Ann. Phys. Chem.* **1859**, *106*, 1.

(8) Rayleigh, L. *Philos. Mag* **1882**, *14*, 184.

(9) Zeleney, J. *Phys. Rev.* **1914**, *3*, 69.

(10) Zeleney, J. *Phys. Rev.* **1917**, *10*, 1.

(11) Gomez, A.; Tang, K. *Phys. Fluids* **1994**, *6*, 404.

(12) Tang, K.; Gomez, A. *Phys. Fluids* **1994**, *6*, 2317.

(13) Hendricks, C. D. *J. Colloid Sci.* **1961**, *17*, 249.

(14) Tafflin, C. D.; Ward, T. L.; Davis, E. J. *Langmuir* **1989**, *5*, 376.

(15) Davis, E. J.; Bridges, M. A. *J. Aerosol Sci.* **1994**, *25*, 1179.

(16) Fernández de la Mora, J. *J. Colloid Interface Sci.* **1996**, *178*, 209.

(17) Taylor, G. I. *Proc. R. Soc. A* **1964**, *280*, 383.

(18) Fernández de la Mora, J. *Annu. Rev. Fluid. Mech* **2007**, *39*, 217.

(19) Rayleigh, L. *Proc. Lond. Math. Soc* **1878**, *10*, 4.

(20) Rayleigh, L. *The Theory of Sound*; Dover: New York, 1945; Chapter XX.

(21) Plateau, J. A. F. *Statique experimentale et theorique des liquids soumis aux seules forces moleculaires*; Gauthiers-Villars: Paris, 1872; Vol. II.

(22) Dole, M.; Mack, L. L.; Hines, R. L.; Mobley, R. C.; Ferguson, L. P.; Alice, M. B. *J. Chem. Phys.* **1968**, *49*, 2240.

(23) Dole, M. *My Life in the Golden Age of America*; Vantage Press: New York, 1989.

(24) Iribarne, J. V.; Thomson, B. A. *J. Chem. Phys.* **1976**, *64*, 2287.

(25) Thomson, B. A.; Iribarne, J. V. *J. Chem. Phys.* **1979**, *7164*, 4451.

(26) Loscertales, I. G.; Fernández de la Mora, J. *J. Chem. Phys.* **1995**, *103*, 5041.

(27) Katta, V.; Rockwood, A. L.; Vestal, M. L. *Int. J. Mass Spectrometry Ion Processes* **1991**, *103*, 129.

(28) Fenn, J. B.; Rosell, J.; Meng, C. K. *J. Am. Soc. Mass Spectrom.* **1987**, *8*, 1147.

(29) Prewett, P. D.; Mair, G. L. R. *Focused ion beams from liquid metal ion sources*; Wiley: New York, 1991.

(30) Bocanegra, R.; Fernández de la Mora, J.; Gamero-Castaño, M. *J. Prop. Power* **2004**, *20*, 728.

(31) Huberman, M. N. *J. Appl. Phys.* **1970**, *41*, 578.

(32) Stimpson, B. P.; Simons, D. S.; Evans, C. A. *J. Phys. Chem.* **1978**, *82*, 660.

(33) Cloupeau, M.; Prunet-Foch, B. *J. Aerosol Sci.* **1994**, *25*, 1021.

(34) Fernández de la Mora, J. *J. Fluid Mech.* **1992**, *243*, 564.

(35) Fernández de la Mora, J.; Loscertales, I. G. *J. Fluid Mech.* **1994**, *260*, 155.

(36) Gañan-Calvo, A. M.; Lasheras, J. C.; Davila, J.; Barrero, A. *J. Aerosol Sci.* **1994**, *25*, 1121.

(37) Rosell-Llompart, J.; Fernandez de la Mora, J. *J. Aerosol Sci.* **1994**, *25*, 1093.

(38) Gañan-Calvo, A. M. *J. Fluid Mech.* **1997**, *335*, 165.

(39) Gañan-Calvo, A. M. *J. Aerosol Sci.* **1999**, *30*, 863.

(40) Gamero-Castaño, M.; Aguirre-de-Carcer, I.; de Juan, L.; Fernández de la Mora, J. *J. Appl. Phys.* **1998**, *83*, 2428.

(41) Gamero-Castaño, M.; Fernández de la Mora, J. *J. Chem. Phys.* **2000**, *113*, 815.

(42) Lozano, P.; Martinez-Sánchez, M. 38th AIAA/ASME/SAE/ASEE Joint Propulsion Conference & Exhibit, Indianapolis, IN, 2002.

(43) Gamero-Castaño, M. *Phys. Rev. Lett.* **2002**, *89*, 147602.

(44) Gañan-Calvo, A. M. *Phys. Rev. Lett.* **1997**, *79*, 217.

(45) Romero-Sanz, I.; Bocanegra, R.; Fernandez de la Mora, J.; Gamero-Castano, M. *J. Appl. Phys.* **2003**, *94*, 3599.

(46) Gamero-Castaño, M.; Hruby, V. *J. Prop. Power* **2001**, *17*, 977.

(47) Chiu, Y.; Austin, B. L.; Dressler, R. A.; Levandier, D.; Murray, P. T.; Lozano, P.; Martinez-Sanchez, M. *J. Prop. Power* **2005**, *21*, 416.

(48) Lozano, P.; Martinez-Sanchez, M. *J. Colloid Interface Sci.* **2005**, *282*, 415.

(49) Lozano, P. *J. Phys. D: Appl. Phys.* **2006**, *39*, 126.

(50) Velasquez-Garcia, L. F.; Martinez-Sanchez, M.; Akinwande, A. I. 40th AIAA/ASME/SAE/ASEE Joint Propulsion Conference and Exhibit, Fort Lauderdale, FL, 2004.

(51) Chiu, Y.; Dressler, R. A. *Ionic Liquids for Space Propulsion. In Ionic Liquids: Not Just Solvents Anymore*; Rogers, R., Ed.; American Chemical Society: Washington, DC, 2006.

(52) Chiu, Y.; Gaeta, G.; Levandier, D. J.; Dressler, R. A. *Int. J. Mass Spectrom.* **2007**, *265*, 146.

(53) Knipping, E. M.; Lakin, M. J.; Foster, K. L.; Jungwirth, P.; Tohias, D. J.; Gerber, R. B.; Dabdub, D.; Finlayson-Pitts, B. J. *Science* **2000**, *288*, 301.

(54) Jungwirth, P.; Tobias, D. J. *J. Phys. Chem. B* **2001**, *105*, 10468.

(55) Jungwirth, P.; Tobias, D. J. *J. Phys. B* **2002**, *106*, 6361.

(56) Brown, E. C.; Mucha, M.; Jungwirth, P.; Tohias, D. J. *J. Phys. Chem. B* **2005**, *109*, 7934.

(57) Mucha, M.; Frigato, T.; Levering, L. M.; Allen, H. C.; Tohias, D. J.; Dang, L. X.; Jungwirth, P. *J. Phys. Chem. B* **2005**, *109*, 7617.

(58) Dang, L. X. *J. Phys. Chem. B* **2002**, *106*, 10388.

(59) Dang, L. X.; Chang, T. M. *J. Phys. Chem. B* **2002**, *106*, 235.

(60) Ghosal, S.; Hemminger, J. C.; Bluhm, H.; Mun, B. S.; Hebenstreit, E. L. D.; Ketteler, G.; Ogletree, D. F.; Requejo, F. G.; Salmeron, M. *Science* **2005**, *307*, 563.

(61) Raymond, E. A.; Richmond, G. L. *J. Phys. Chem. B* **2004**, *108*, 5051.

(62) Liu, D. F.; Ma, G.; Levering, L. M.; Allen, H. C. *J. Phys. Chem. B* **2004**, *108*, 2252.

(63) Petersen, P. B.; Johnson, J. C.; Knutsen, K. P.; Saykally, R. J. *Chem. Phys. Lett.* **2004**, *397*, 46.

(64) Petersen, P. B.; Saykally, R. J. *Chem. Phys. Lett.* **2004**, *397*, 51.

(65) Petersen, P. B.; Saykally, R. J. *J. Am. Chem. Soc.* **2005**, *127397*, 15446.

(66) Petersen, P. B.; Saykally, R. J. *Annu. Rev. Phys. Chem.* **2006**, *57*, 12–1.

(67) Petersen, P. B.; Saykally, R. J.; Mucha, M.; Jungwirth, P. *J. Phys. Chem. B* **2005**, *109*, 10915.

(68) Znamenskiy, V.; Marginean, I.; Vertes, A. *J. Phys. Chem. A* **2003**, *107*, 7406.

(69) Moseler, M.; Landman, U. *Science* **2000**, *289*, 1165.

(70) Kang, W.; Landman, U. *Phys. Rev. Lett.* **2007**, *98*, 064504.

(71) Duft, D.; Achtzehn, T.; Müller, R.; Huber, B. A.; Leisner, T. *Nature* **2003**, *421*, 128.

(72) Duft, D.; Lehius, H.; Huber, B. A.; Guet, C.; Leisner, T. *Phys. Rev. Lett.* **2002**, *89*, 084503.

(73) Grimm, R. L.; Beauchamp, J. L. *J. Phys. Chem. B* **2005**, *109*, 8244.

(74) Grimm, R. L.; Beauchamp, J. L. *J. Phys. Chem. B* **2003**, *107*, 14161.

(75) Stone, H. A.; Lister, J. R.; Brenner, M. P. *Proc. R. Soc. London A* **1999**, *455*, 329.

(76) Greengard, L. F. *The rapid evaluation of potential fields in particle systems*; The MIT Press: Cambridge, MA, 1988.

(77) Allen, M. P.; Tildesley, D. J. *Computer simulation of liquids*; Clarendon: Oxford, 1987.

(78) Svanberg, M. *Mol. Phys.* **1997**, *92*, 1085.

(79) Stevens, E. D. *Acta Crystallogr.* **1978**, *B34*, 544.

(80) Cornell, W. D.; Cieplak, P.; Bayly, C. I.; Gould, I. R. K. M.; Merz, J.; Ferguson, D. M. C.; Spellmeyer, D.; Fox, T.; Caldwell, J. W.; Kollman, P. A. *J. Am. Chem. Soc.* **1995**, *117*, 5179.

(81) Sigfridsson, E.; Ryde, U. *J. Comput. Chem.* **1998**, *19*, 377.

(82) Perera, L.; Essmann, U.; Berkowitz, M. L. *J. Chem. Phys.* **1994**, *102*, 450.

(83) Frisch, M. J. ; Trucks, G. W.; Schlegel, H. B.; Scuseria, G. E.; Robb, M. A.; Cheeseman, J. R.; Montgomery, J. A., Jr.; Vreven, T.; Kudin, K. N.; Burant, J. C.; Millam, J. M.; Iyengar, S. S.; Tomasi, J.; Barone, V.; Mennucci, B.; Cossi, M.; Scalmani, G.; Rega, N.; Petersson, G. A.; Nakatsuji, H.; Hada, M.; Ehara, M.; Toyota, K.; Fukuda, R.; Hasegawa, J.; Ishida, M.; Nakajima, T.; Honda, Y. ; Kitao, O.; Nakai, H.; Klene, M.; Li, X.; Knox, J. E.; Hratchian, H. P.; Cross, J. B.; Bakken, V.; Adamo, C.; Jaramillo, J.; Gomperts, R.; Stratmann, R. E.; Yazyev, O.; Austin, A. J.; Cammi, R.; Pomelli, C.; Ochterski, J. W.; Ayala, P. Y.; Morokuma, K.; Voth, G. A.; Salvador, P.; Dannenberg, J. J.; Zakrzewski, V. G.; Dapprich, S.; Daniels, A. D.; Strain, M. C.; Farkas, O.; Malick, D. K.; Rahuck, A. D.; Raghavachari, K.; Foresman, J. B.; Ortiz, J. V.; Cui, Q.; Baboul, A. G.; Clifford, S.; Cioslowski, J.; Stefanov, B. B.; Liu, G.; Liashenko, A.; Piskorz, P.; Komaromi, I.; Martin, R. L.; Fox, D. J. K.T.; Al-Laham, M. A.; Peng, C. Y.; Nanayakkara, A.; Challacombe, M.; Gill, P. M. W.; Johnson, B.; Chen, W.; Wong, M. W.; Gonzalez, C.; Pople, J. A. *Gaussian 03*, revision C.02; Gaussian, Inc.: Wallingford, CT, 2004.

(84) Kendall, R. A.; Dunning, T. H., Jr.; Harrison, R. J. *J. Chem. Phys.* **1992**, *96*, 6796.

(85) Hariharan, P. C.; Pople, J. A. *Theor. Chim. Acta.* **1973**, *28*, 213.

(86) Glukhovtsev, M. N.; Pross, A.; Radom, L. *J. Am. Chem. Soc.* **1995**, *117*, 2024.

(87) Becke, A. D. *J. Chem. Phys.* **1993**, *98*, 5648.
(88) Hertwig, R. H.; Wolfram, K. *Chem. Phys. Lett.* **1997**, *268*, 345.
(89) Stephens, P. J.; Devlin, F. J.; Chabalowski, C. F.; Frisch, M. J. *J. Phys. Chem.* **1994**, *98*, 11623.
(90) Frisch, M. J.; Head-Gordon, M.; Pople, J. A. *Chem. Phys. Lett.* **1990**, *166*, 275.
(91) Pople, J. A.; Binkley, J. S.; Jeeger, R. *Int. J. Quantum Chem. Symp.* **1976**, *10*, 1.
(92) Aikens, C. M.; Webb, S. P.; Bell, R. L.; Fletcher, G. D.; Schmidt, M. W.; Gordon, M. S. *Theor. Chem. Acc.* **2003**, *110*, 233.
(93) Krishnan, R.; Binkley, J. S.; Seeger, R.; Pople, J. A. *J. Chem. Phys.* **1980**, *72*, 650.
(94) Glukhovtsev, M. N.; Pross, A.; McGrath, M. P.; Radom, L. *J. Chem. Phys.* **1995**, *103*, 1878.
(95) Gordon, M. S.; Schmidt, M. W. In *Advances in Electronic Structure Theory: GAMESS a Decade Later. In Theory and Applications of Computational Chemistry*; Dykstra, C. E., Frenking, G., Kim, K. S., Scuseria, G. E., Eds.; Elsevier: Amsterdam, 2005.
(96) Sch, M. W.; Baldridge, K. K.; Boatz; J. A.; Elbert, S. T.; Gordon, M. S.; H., J. J.; S., K.; Matsunaga, N.; Nguyen, K. A.; Su, S.; Windus, T. L.; Dupuis, M.; Montgomery, J. A. *J. Comput. Chem.* **1993**, *14*, 1347.
(97) Zhu, L.; Chen, W.; Hase, W. L.; Kaiser, E. W. *J. Phys. Chem.* **1993**, *97*, 311.
(98) Rodgers, M. T.; Ervin, K. M.; Armentrout, P. B. *J. Chem. Phys.* **1997**, *106*, 4499.
(99) Beyer, T. S.; Swinehart, D. F. *Comm. Assoc. Comput. Machines* **1973**, *16*, 379.
(100) Luedtke, W. D.; Landman, U. To be published.
(101) Li, D.; Neumann, A. W. *J. Colloid Interface Sci.* **1992**, *148*, 190.
(102) Garrett, B. C. *Science* **2004**, *303*, 1146.
(103) Simons, D. S.; Colby, B. N. C. A.; Evans, J. *Int. J. Mass Spectrom. Ion Phys.* **1974**, *15*, 291.
(104) Perera, L.; Berkowitz, M. L. *J. Chem. Phys.* **1991**, *95*, 1954.
(105) Ayotte, P.; Nielsen, S. B.; Weddle, G. H.; Johnson, M. A.; Xantheas, S. S. *J. Phys. Chem. A* **1999**, *103*, 10665.

JP804585Y